Modelling of Electric Powertrain for Heavy-Duty BEV

Master of Science Thesis

Nived Abhay

TU Delft

Modelling of Electric Powertrain for Heavy-Duty BEV

by

Nived Abhay

to obtain the degree of Master of Science
at the Delft University of Technology,
to be defended publicly on Tuesday August 25, 2020 at 03:00 PM.

Student number:	4899059	
Project duration:	December 1, 2019 – August 25, 2020	
Thesis committee:	Prof. dr. ir. P. Bauer,	TU Delft, Supervisor
	Dr. J. Dong,	TU Delft
	Ir. S. Nouws,	DAF Trucks N. V.
	Dr. ir. J. L. (Jose) Rueda Torres,	TU Delft

This thesis is confidential and cannot be made public until August 25, 2022.

TU Delft

Abstract

The automotive industry plays a crucial role in battling the climate crisis and reducing emissions. Medium-duty and heavy-duty vehicles alone contribute to one-fourth of global emissions in the transport sector and there is a positive trend in the demand for these vehicles. Battery Electric Trucks have the potential to transform the growing logistics industry.

DAF Trucks N.V., one of the largest truck manufacturers in Europe, aims to transition to zero-emission vehicles and advance in this future of electric mobility. This project aims to model the powertrain of their CF Electric model and explore viable options for future designs. The thesis work can be defined in three parts.

The first part of the research focuses on modelling the electric powertrain in MATLAB/Simulink. Here, more focus is given in the calculation of individual motor and inverter losses. These losses are reverse engineered and extracted from the motor drive efficiency map using Particle Swarm Optimisation (PSO) algorithm.

The second part of the project focuses on performing sensitivity analysis to identify the key parameters that have the most influence on the energy efficiency of the Battery Electric Vehicle (BEV). This helps to prioritise and focus on optimisation of these parameters for future models. A comparison is drawn between the percentage change in the range each parameter has with small changes.

Lastly, in the third part of the thesis, different powertrain architectures are studied and modelled to understand their influence on the range of the BEV and the challenges involved in implementing such layouts.

Acknowledgement

Firstly, I would like to express my sincere gratitude to my daily supervisor, Dr. Jianning Dong, for his constant support and guidance throughout the thesis work. His valuable advice and critical feedback has steered me in the right direction and helped me improve the quality of my work. He has motivated and encouraged me during the course of my thesis especially in this pandemic and has always given me timely comments for my work.

I would like to further express my thanks to my supervisor at the company, Ir. Simon Nouws, for giving me the opportunity to work in this exciting project. He has always guided me in the right direction and asked me thought-provoking questions with his sharp observations. I would like to thank him for all the intriguing discussions we had that have helped me reshape the thesis in these difficult times of COVID-19.

I would like to thank Dr. Pavol Bauer for chairing my thesis committee and also Dr. José Rueda Torres for taking the time to access my work as an external member.

Finally, I would like to thank my friends and family for being there for me whenever I needed them. My parents and my sister have been the most loving, patient and supportive people. No amount of words could describe how grateful and lucky I am for everything they have done and sacrificed for me. All my friends have been truly amazing and have shaped me to be who I am today. I would like to express my love for Medha and Newman for all the unforgettable and adventurous memories you have given me ever since I came to the Netherlands. You guys inspire me to think out-of-the-box and challenge myself.

Nived Abhay
Delft, January 2020

Contents

1 Introduction

This chapter serves as an introduction to this thesis work. Section 1.1 addresses the motivation behind this project and the role of electrification in urban heavy-duty trucks. Section 1.2 exemplifies the objectives of the work of this research. Section 1.3 presents the main goals aimed to achieve in this project. Section 1.4 outlines the structure of this thesis.

1.1. Motivation

To battle climate change, researchers, policymakers and industries are working hand-in-hand to facilitate a smooth energy transition and reduce emissions. The automotive industry is a critical player in this energy transition. Medium-duty and heavy-duty vehicles play an important role in global and urban emissions in the transportation sector. To reduce the carbon footprint left by these vehicles, DAF Trucks, one of the largest truck manufacturers in Europe, aims to transition and make its fleet more electric and sustainable.

Electric vehicles have advantages like full torque at zero speed, giving them excellent acceleration compared to the internal combustion engines and has proved to be an ideal alternative to ICE vehicle. Nowadays, more tractor manufacturers are joining the transition and building their medium-duty and heavy-duty battery electric vehicles (BEV). As per the statistics from US Environmental Protection Agency (EPA), 25 per cent of the global emissions in the transportation sector comes from heavy-duty vehicles even though they constitute only 5 per cent of all vehicles [1]. For the same reason, it is of utmost importance to address the pollution caused by heavy-duty vehicles and reduce emissions. Reduction of greenhouse gasses is of considerable significance to improve the air quality [2].

However, the transition is a gradual process. Implementation of an electric powertrain hardware prototype directly can be detrimental to the investment in these projects. Hence, the electric propulsion system is designed and modelled using simulation software to understand the scope of the project better.

Software modelling and testing of proposed electric drive module prototypes enable risk reduction and demonstrate whether or not specific designs are viable in an early stage. This allows for rapid prototyping loops, speeding up the decision-making process while being a low-cost alternative to full-scale prototypes.

1.2. Thesis Objectives

This thesis aims to implement an electric powertrain model of a heavy-duty BEV to understand energy consumption and various electrical losses. Different powertrain designs are also investigated to recognise its effect on energy consumption. Some of the specific objectives are defined below:

- Develop a heavy-duty BEV model based on mathematical equations and predict energy consumption over a pre-defined driving cycle.
- Build a motor and inverter model and extract information such as individual power losses from only an efficiency map.
- Perform sensitivity analysis to identify the key parameters that influence the driving range of the BEV.
- Compare energy consumption for different powertrain architectures: the single motor with fixed reduction gear, the dual-motor with AWD and two-speed transmission.

1.3. Research Questions

In order to realise the above-listed objectives, certain research questions arise, and they are formulated as listed below

- How can the motor and inverters losses be extracted from an existing efficiency map to analyse the power consumption of the powertrain?
- What are the key parameters that have a significant effect on the energy efficiency of the heavy-duty BEV?
- What impacts do different powertrain architectures have on energy consumption on the BEV?

1.4. Methodology

The environment used for modelling and simulation purpose in this project is MATLAB Simulink. The approach taken to understand the power consumption of the heavy-duty BEV can be listed as follows.

- The heavy-duty truck and its parameters are identified, and mathematical equations are used to model the truck dynamics.
- Using the efficiency map of the motor drive used in the existing BEV, individual motor and inverter losses are extracted using optimisation algorithms.
- A regenerative braking logic is used to recuperate maximum energy during the braking operation. Based on the final model, simulations are run to analyse the energy efficiency and operating points of the motor drive.
- A sensitivity analysis is conducted by varying different parameters of the truck to observe the optimal value to achieve maximum range.
- Different powertrain architectures are also studied and modelled to investigate the difference in energy efficiencies compared to a single motor with reduction gear powertrain. This study also helps to demonstrate the viability of different powertrain options with minimal changes for future research.

1.5. Thesis Outline

The thesis is written in 7 chapters. This chapter is the introduction to the project with research questions and goals listed. Chapter 2 gives the background information required to understand the model and the approach taken to achieve the research objective.

Chapter 3 explains the motor modelling with a focus on the loss calculation and efficiency map. In this chapter, an evolutionary optimisation algorithm is introduced to obtain an accurate model. Chapter 4 illustrates the approach taken to estimate the losses contributed by the inverter and outline the overall electrical drive layout. Chapter 5 presents the results from performing sensitivity analysis and identifies the key parameters that have a significant impact on the BEV range.

Chapter 6 presents the performance results from the implementation of various powertrain architectures and provide suggestions on future research direction. Chapter 7 ends the report with the conclusion and future recommendation of the research work.

2

Overview of Electric Powertrain

This chapter focuses on presenting the background information and the modelling approach taken to build a MATLAB Simulink model of a heavy-duty battery electric vehicle (HD-BEV). Firstly, the system and the vehicle's resistive forces are defined, followed by a discussion on the simulation approach. Next, the modelling of the powertrain is explained with the specifics on the calculation of energy consumption. Finally, the different powertrain architectures that are interesting for the future medium-duty and heavy-duty trucks are introduced, and possibilities of implementation on the current model are examined.

2.1. System Overview - Heavy-Duty Battery Electric Vehicle

Heavy-Duty Battery Electric Vehicle (HD-BEVs) has recently gained traction in becoming a viable and zero-emission alternative to diesel-fuelled trucks [3]. The truck modelled in this thesis is based on an existing BEV powertrain designed for a wide variety of urban distribution applications requiring heavy payloads and volumes.

These HD-BEVs are also suitable for applications such as supermarket delivery, where single or double axle semi-trailers are the standard [4]. The modelled electric tuck is a 4x2 RWD (Rear-Wheel-Drive) tractor unit with a capacity for up to 37-ton GCW applications [5]. The Gross Combination Mass (GCM) is the combined weight of the truck and the trailer with full load. The truck is powered by the 200 kW/268 hp electric motor with a peak of 240 kW/326 hp. This motor is modelled in chapter 3. In later chapters, for analysis purposes, a battery pack of 150kWh is considered though this is not as per the original design of the truck.

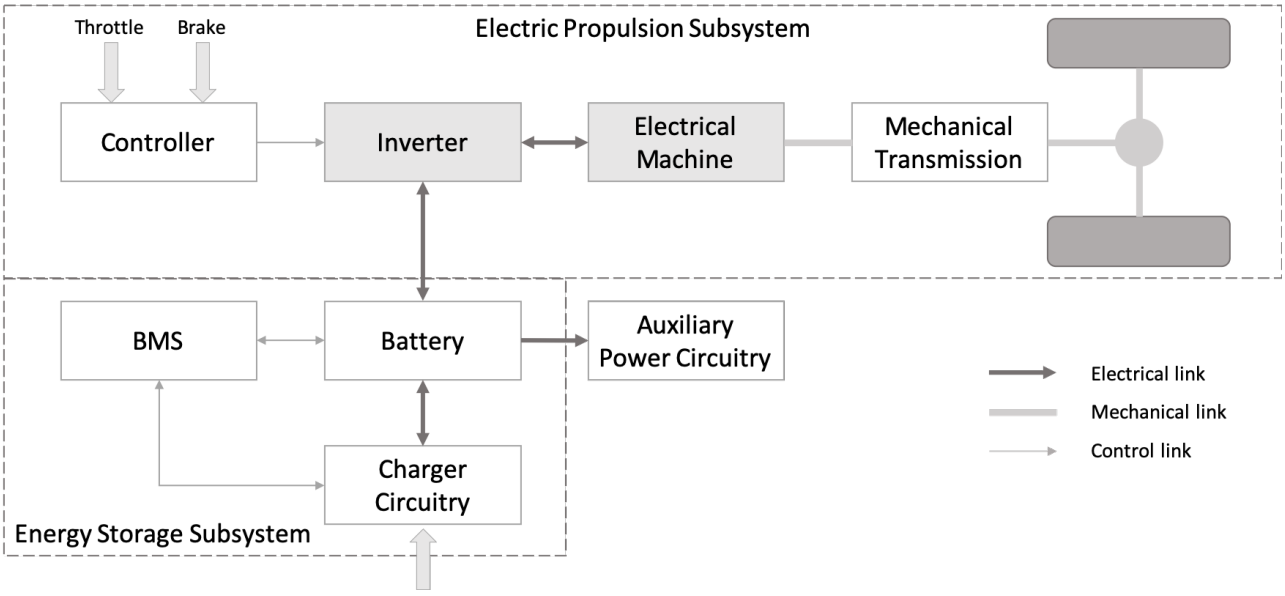

Figure 2.1: General Layout of the Electric Powertrain [6]

A general layout of the electric powertrain of these BEVs can be seen in figure 2.1 [6]. In this figure, two subsystems are presented, namely - Electric Propulsion and Energy Storage Subsystems. Electric propulsion

subsystem comprises of the electrical motor, inverter and the controller while the energy storage subsystem includes of the battery, Battery Management System (BMS) and charger circuitry. Some of the additional modules that play a significant role are in the energy consumption of the BEV are auxiliary power circuitry and mechanical transmission. As the focus of this thesis is on analysing the energy efficiency and impact of the powertrain elements, the primary focus will be on the electric propulsion subsystem.

2.2. Truck Resistive Forces

It is essential to understand the truck dynamics in order to analyse vehicle performance and energy consumption effectively. In this powertrain design and simulation, a simplified vehicle dynamics model, only in the longitudinal forward direction, is taken assuming the vehicle will be stable at all conditions.

In this project, a rear-wheel-drive truck is chosen. The energy flows from the motor to the wheel via a single-speed transmission and a differential. The primary elements in an electric powertrain are (i) electric motor drive, (ii) transmission and (iii) axle shaft.

While driving, the vehicle experiences three major opposing forces which the traction has to overcome to move the vehicle forward. The opposing forces are rolling resistance, aerodynamic drag and grading force. These forces experience by the truck, as seen in 2.2, are further explained below. In simple terms, the vehicle will accelerate if the tractive force $F_{tractive}$ is greater than the resistive force $F_{resistive}$ and will decelerate if $F_{tractive}$ is lesser than $F_{resistive}$. It will remain in steady speed when both the forces cancel each other out [7].

$$F_{net} = F_{tractive} - F_{resistive}$$

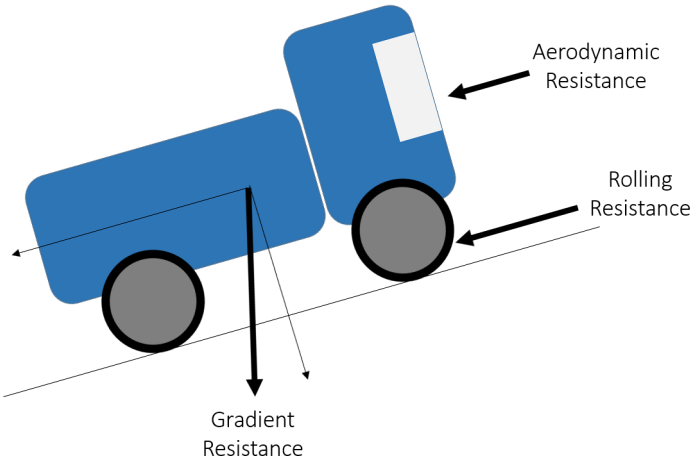

Figure 2.2: Graphical representation of the resistive forces experienced by the truck

2.2.1. Rolling Resistance F_r

Repeated deflection of the tires causes a hysteresis within the tire material, which gives rise to an internal force resisting the motion of the tire [8]. This force is the rolling resistance, and they are always opposing the vehicle motion. The rolling resistance is calculated using,

$$F_r = C_r M g \cos\theta \tag{2.1}$$

where,

C_r is the coefficient of resistance
M is the mass of the vehicle
g is the acceleration due to gravity
θ is the slope of the road surface.

2.2.2. Aerodynamic Resistance F_{aero}

Aerodynamic resistance is the impact the airflow has on the vehicle as it accelerates to higher speeds. These forces are a significant factor in vehicle dynamics as they cause drag, lift, lateral forces, moments in roll, pitch and yaw and noises.The aerodynamic forces have a notable influence in the vehicle range, handling and NVH

(Noise, vibration and harshness) performance [9]. This resistance is due to pressure drag and viscous friction. Since it is highly linked with the dynamic pressure drag, it is proportional to the square of the vehicle speed as seen in the equation below.

$$F_{aero} = \frac{\rho}{2} C_d A_f (v_{truck} - v_{wind})^2 \tag{2.2}$$

where,

ρ is the air density

C_d is the drag coefficient

A_f is the frontal area

v_{truck} and v_{wind} are the velocities of the truck and wind respectively. Note that the wind velocity is neglected in the simulation.

2.2.3. Gradient Resistance F_g

The gradient resistance of the road can be positive (uphill) or negative (downhill) and this would define if it accelerates or decelerates the vehicle. The grade is defined as the rise over the run (vertical over horizontal distance) [9]. The gradient resistance experienced by the truck can be calculated using,

$$F_g = Mg \sin\theta \tag{2.3}$$

2.3. Simulation Approach

Two approaches are taken to simulate a powertrain of a vehicle model [10]. These two approaches follow the building of forward-facing and backward-facing models.

Backward-facing models use drivecycle information to obtain the vehicle speed, and they do not have a driver model. The speed profile is used on the vehicle model to calculate the velocity and torque at the motor. They are considered ”quasi-static” models as they utilise efficiency-maps obtained from steady-state testing of real components. For the same reason, these models provide limited information about the driveability of the vehicle [4]. Whereas, forward-facing models are known to give more insight into the dynamics and physical limits of the powertrains [11][12].

It is of general understanding that for control system development and hardware-in-the-loop (HIL) test systems, the quasi-static nature of backward-facing models is less suitable compared to the nature of the forward-facing model [10].

2.3.1. Forward-facing Model

The topology of the forward-facing model is shown in figure 2.3. In this model, the drivecyle data is given as an input which is used by the driver model to provide acceleration and brake demands to the motor model. The input drivecycle is speed versus time trace data. The motor model provides the information of the torque delivered by the motor, which includes the physical limits of the component as well. This torque flows through the transmission and final drive ratio and provides the necessary force to make the vehicle trace the speed from the drivecyle. Each of these modules is discussed further in the next section.

It can be noticed that the vehicle speed is propagated back through the drive train as this helps us calculate the angular velocity at the motor. In backward-facing models, the speed trace is imposed onto the vehicle model. As that is not the case in forward-facing models, there is an error between the reference speed and the actual speed of the vehicle. The driver model’s role is to minimise this error. However, this behaviour is similar to a real-world driver carrying out the test and hence the name.

As forward simulation utilises multiple state-equations, it gives insight into the physical limits and dynamics of the vehicle model [10]. A drawback this type of simulation imposes is that the driver model may require to be returned when powertrain components are resized to maximise the system performance.

Another feature that the forward simulation is made to perform here is the calculation of real bidirectional power flow between the energy storage unit and the electric motor [13] [14].

2.3.2. Backward-facing Model

Backward-facing model works under the assumption that the vehicle model can meet the speed requirements of the drivecyle [11]. In this simulation approach, the vehicle block calculates the force required at the wheels to follow the speed trace from the drive cycle. This force and speed is fed to the transmission block where it converted to the torque and rotational speed provided by the motor [14][13].

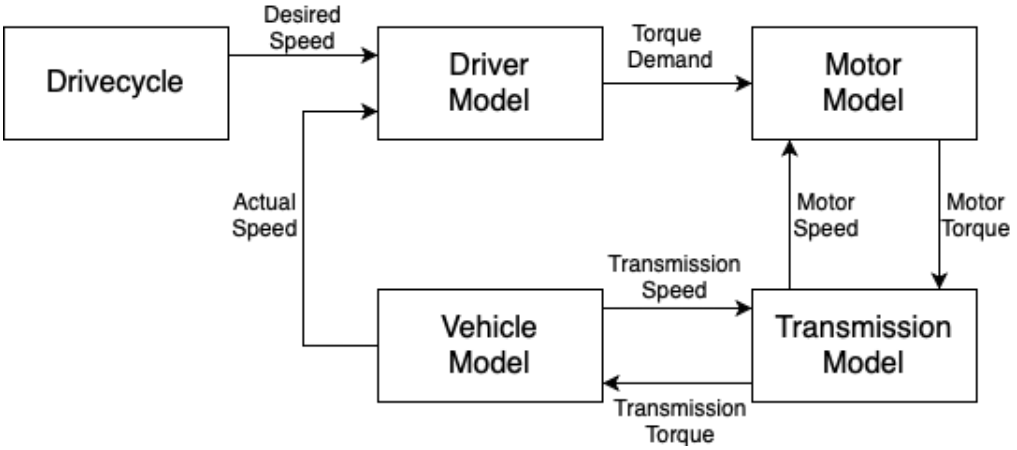

Figure 2.3: Forward-facing Vehicle Model [10]

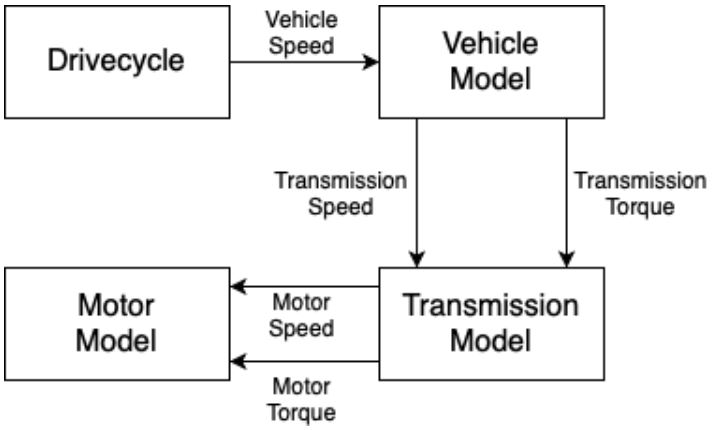

Figure 2.4: Backward-facing Vehicle Model [10]

Thus this approach can be considered non-causal (acausal), as both the torque and speed are imposed to the powertrain components. The acausal nature and inability to capture system dynamics make the backward-facing models very difficult to be implemented in HIL systems and control system development [10]. Hence, the forward-facing simulation approach will be considered for the modelling of the powertrain of heavy-duty BEV.

2.4. Powertrain Model Development

In this section, the step-by-step approach taken in the modelling of the powertrain is explained. The figure 2.5 shows the overall structure of the final powertrain model. In this figure, the black lines represent the flow of mechanical related signals such as pedal inputs, drive torques and vehicle speeds. The blue line represents the bidirectional flow of electrical energy to and from the motor during driving and regenerative braking. It is essential to understand this structure as the aim of this model is to estimate the energy efficiency of the HD-BEV. The integral of the power drawn from and fed to the battery gives us the information about the net energy utilised. Because of the same, it is significant to understand losses at each of the powertrain components to estimate energy efficiency with utmost accuracy.

2.4.1. Driver Model

The idea of understanding the behaviour of the driver was introduced in the 1960s. In the past couple of decades, more research is being conducted specifically due to the growth of self-driving technology. One of the widely used and popular approaches is the preview-follower theory which was put forth by Guo and Fancher in [15]. According to this theory, the driver's behaviour in a path following system is aimed at reducing the error between the desired speed and actual speed of the vehicle. This operation can be modelled using a PI controller [15] as seen in the figure 2.6.

In a practical scenario, a driver's pedal input signal is dependent on various factors surrounding the driver and the vehicle. A PI controller is used to mimic the input by analysing the amount of acceleration or brake

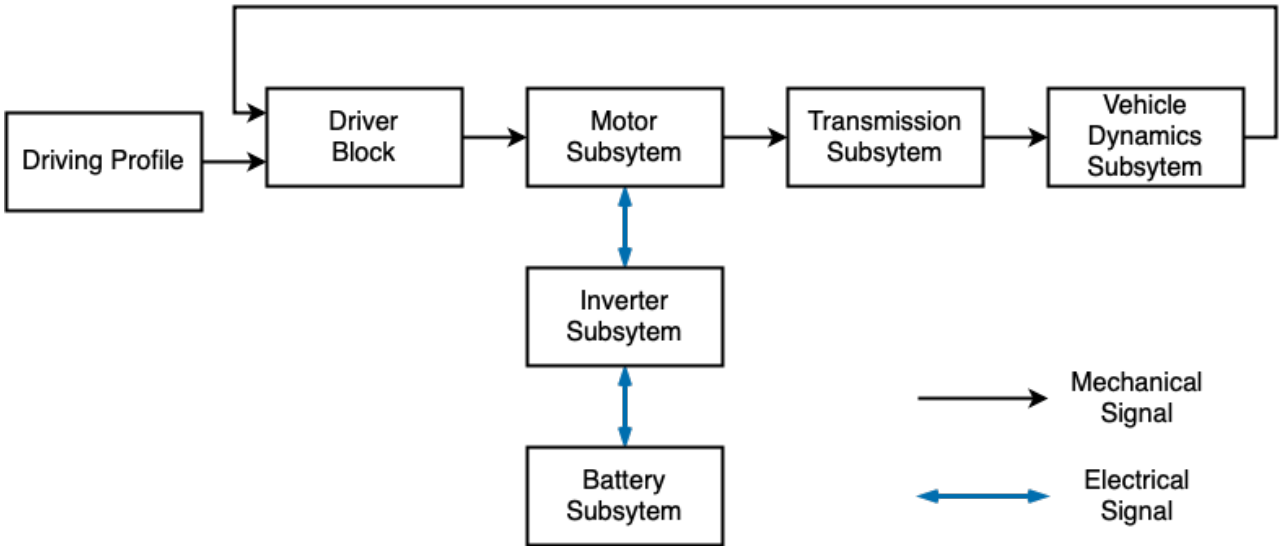

Figure 2.5: Block diagram representing the outlook of the overall powertrain model

that is required to attain the reference speed. To implement this model, firstly, the error difference between the reference speed and the actual speed of the vehicle is calculated. This error signal is used to estimate the acceleration and the brake input to the vehicle. The error signal is fed to a PI controller with the gain constants K_p and K_i representing the proportional and integral gains. The PI controller is tuned in such a manner that the error signal is minimum with no oscillations.

The output signal from the PI controller is then fed to a saturation block to limit the pedal signals at a range -100 to +100 in terms of percentage of the pedal input applied. The positive value corresponds to the acceleration pedal signal, while the negative values correspond to the brake pedal signal [10]. The pedal signals are fed to the motor block to determine the drive torque and brake torques.

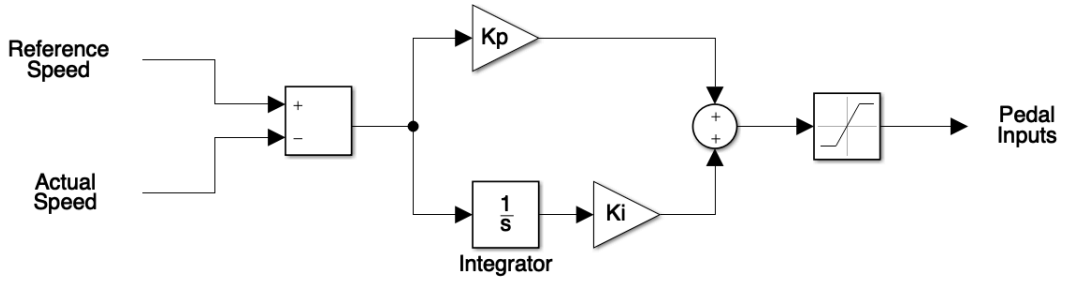

Figure 2.6: Driver Subsystem

2.4.2. Motor Model

Permanent Magnet Synchronous Motors are the most common motors used in the automotive industry for both battery-electric and hybrid vehicles. The primary reason for the popularity of this motor is its high torque density and high-efficiency [16][17]. Having high torque density helps reduce the overall size and weight of the vehicle and having high efficiencies help to maximise the achievable range in BEVs.

In this project, a permanent magnet synchronous motor from the Siemens ELFA series is modelled, and its efficiency map is used to evaluate the input power at various operating points of the machine. This modelling concept is depicted in the figure 2.7 and it is further explained in detail in chapter 3. The depicts the electrical power flow in the model.

Additionally, the amount of torque delivered by the motor to the wheels is calculated from the pedal inputs from the driver model. The amount of torque is determined based on the torque limit and speed of the motor. This subdivision represents the flow of mechanical power from the motor.

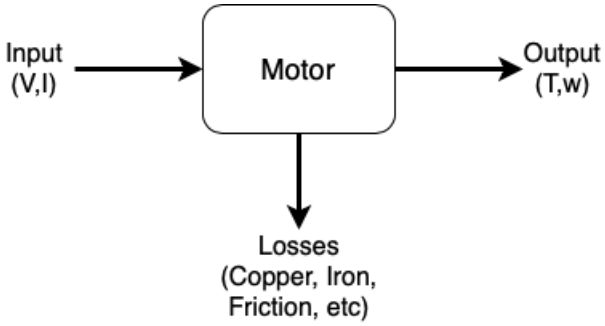

Figure 2.7: Motor modelling concept based on efficiency map [18]

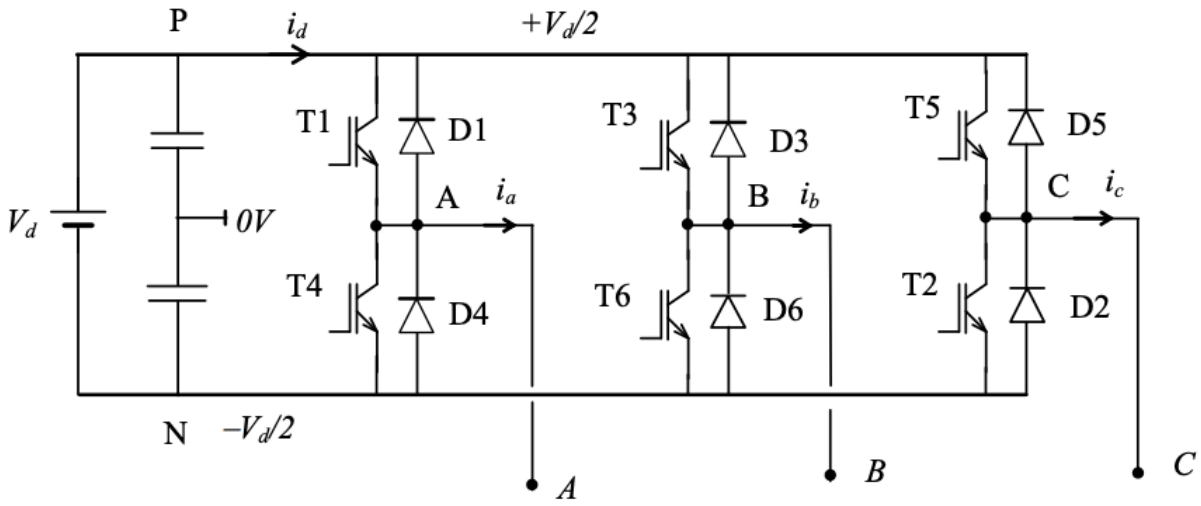

Figure 2.8: Topology of a 2 level 3 phase inverter

2.4.3. Inverter Model

The inverter used in this motor drive of the powertrain system is a 2-level 3 phase inverter with six bidirectional switching modules. Each module consists of an IGBT and a diode connected in antiparallel to each other [13]. Figure 2.8 shows the structure of the 2-level 3 phase inverter. The term V_d represents the DC voltage from the battery, and the terminals A, B and C portrays the three terminals of the three-phase PMSM used in the powertrain.

The inverter model is incorporated in this model to understand the switching and conduction losses and estimate the inverter efficiency in the entire duration of the operation. The modelling of the inverter is explained in detail in chapter 4. The output of this model built represents the power from the battery. Moreover, constant power is assumed to be drawn by the auxiliary system in the HD-BEV. This feature is also included in the model.

2.4.4. Transmission

The heavy-duty vehicle modelled is an RWD (Rear-Wheel Drive) vehicle which means that the power from the motor is delivered to the rear axle. Here, a single-speed transmission with a fixed ratio gear along with differential is used for this purpose. The single compact assembly makes this type of transmission an attractive choice for BEVs [19]. However, due to the efficiencies of gear and differential, the powertrain experiences some mechanical losses. Hence, the wheels do not receive the total tractive torque from the motor.

Equations 2.4 and 2.5 express the tractive force generated by the motor on driven wheels and the vehicle speed. It can be seen that the motor's torque-speed characteristics is a defining element in the selection of multi-gear or single-gear transmission. If the motor has a broad constant power region and the motor can be operated over its speed range to reach desired vehicle speeds, then a single-gear transmission will suffice [20].

$$F_w = \frac{T_m \times GR \times \eta_{GR}}{r_w} \tag{2.4}$$

$$V = \frac{2\pi}{60}\frac{\omega_m r_w}{GR} \tag{2.5}$$

Here,
F_w is the force at the wheels
T_m is the motor torque
GR is the gear ratio of the reduction gear between motor and wheels
η_{GR} is the efficiency of the driveline from the motor to the wheels
r_w is the radius of the wheels
V is the velocity of the vehicle and
ω_m is the rated speed of the motor

2.4.5. Truck Dynamic Model

Based on the resistance forces that the HD-BEV has to overcome, a Simulink model is built with the above discussed mathematical equations. The force provided by the motor should overcome the resistance forces and this force at the wheels determine the driving force of the vehicle. From Newton's second law of motion, it is known that the force is equal to the product of mass times acceleration. Hence, dividing the driving force with the mass of the heavy-duty vehicle, the acceleration is obtained, and integration of acceleration gives the velocity of the vehicle. All the values here are taken in SI units for the simulations.

A power consumption model is built, which gives us the following information: power consumption, net energy used, distance travelled, and the energy efficiency achieved. The power consumption is the power at the battery during driving and braking conditions. The area under the power curve gives the total energy consumed for the entire cycle. Thus the net energy is calculated by integrating power. Integration of velocity gives the displacement, and this helps to estimate the range and energy efficiency of the BEV. Energy efficiency is net energy divided by the distance travelled and hence is represented in kWh/km.

The vehicle parameters of the electric truck are listed in table 2.1. Most of these parameters are taken from the openly available information of the truck [21][22][23] and remainder from internal sources. Hence, confidential information is written in per-unit value (p.u.). For example, the value of the coefficient of friction is a range with a maximum and minimum. An average is taken, and per-unit of the range of values from maximum to minimum is calculated. These different per-unit values of the different parameters will be used to discuss the results from the sensitivity analysis in chapter 5.

Parameter	Value	Unit	Source
Mass of the Truck (GCM)	37000	Kg	Truck Specification
Mass of the Tractor (GVM)	9700	Kg	Truck Specification
Tire Coefficient of Friction	1	p.u.	Truck Specification
Aerodynamic Drag Coefficient (with aerodynamic aids)	1	p.u.	Truck Specification
Aerodynamic Drag Coefficient (without aerodynamic aids)	1.41	p.u.	Truck Specification
Frontal Area of the truck	7.2	m^2	Truck Specification
Wheel Radius	0.4748	m	Truck Specification
Gear Ratio	7.21	-	Truck Specification
Gear box efficiency	1	p.u.	Truck Specification
Road Gradient	0 (variable)	rad	

Table 2.1: Truck dynamics parameters of the heavy-duty BEV

2.5. Powertrain Architectures

An electric powertrain is described as the heart of a BEV [24]. It comprises of electrical motor and its power converters. There are many battery electric vehicles (BEVs) in the market today, and each of them uses different electrical machines in their powertrains. The single-motor powertrain utilised in a typical battery-electric truck is represented in figure 2.9 for clear understanding. This figure helps to understand the assembly and visualise the electrical power flow from the charger and the motor.

The electrical power flow starts from the battery, which stores energy chemically. The power from the battery is transferred to the motor via the inverter driven by a control system. The control system regulates the amplitude and frequency of the supply to manipulate the motor to respond as per the driver's pedal input.

In recent years, electric vehicle technology has developed incredibly with numerous powertrain topologies. These powertrains can be classified based on the number of motors and type of transmission. Some of the

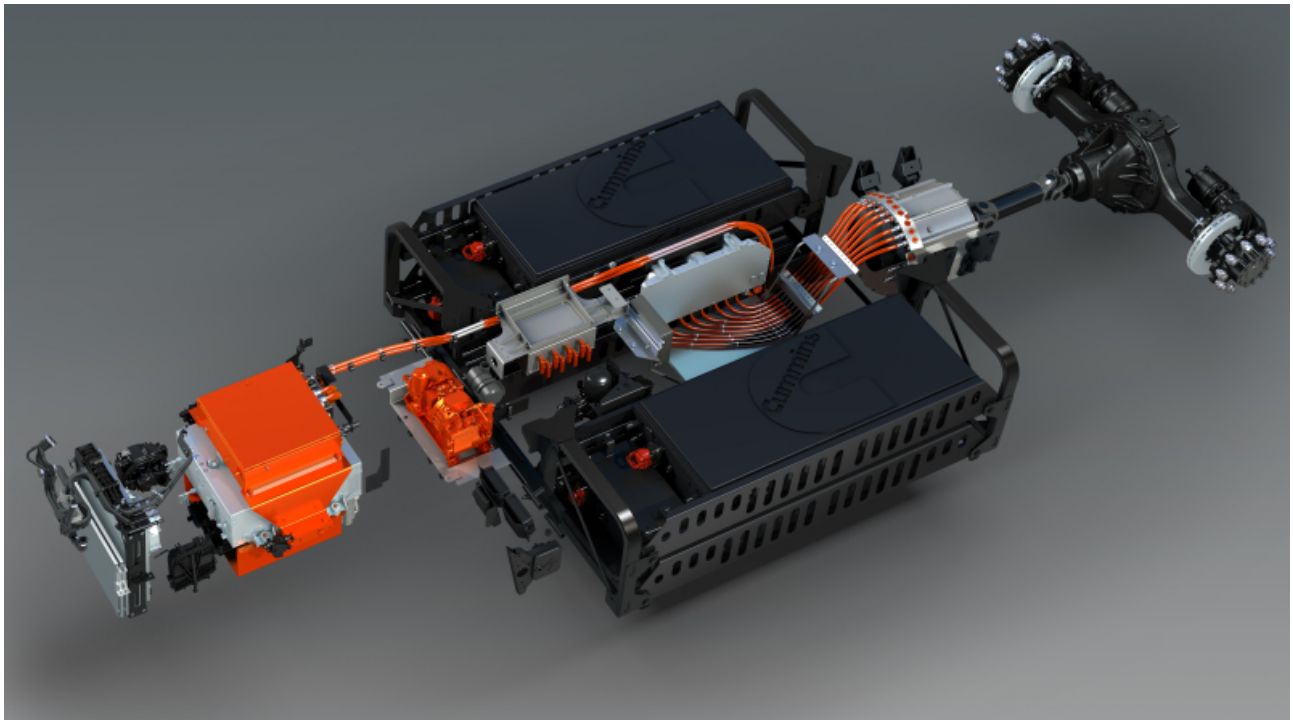

Figure 2.9: Heavy-Duty BEV Powertrain highlighting the Electrical Components [4]

topologies include single-motor driven powertrain, dual-motor powertrain, multi-motor distributed powertrain, two-speed single motor powertrain, and in-wheel drive [25]. In this section, these powertrain architectures will be addressed.

2.5.1. Single Motor Powertrain System

A single motor powertrain with a single-speed reduction gear is the most straightforward layout in the electric vehicles sector. This architecture of the powertrain is widely adopted in the automotive industry because of the cost-effectiveness, compactness, and reduced transmission losses [19].

Some of these advantages are significant as they have a direct impact on the range of the BEV. A compact powertrain reduces the weight of the overall vehicle, which can be compensated with supplementary cells to provide more energy. Furthermore, less number of transmission components increases the overall efficiency of the powertrain. This simple layout also has shortcomings. When the electric motor operates at very low or very high speeds, the efficiency is inferior compared to the rest of the operating region.

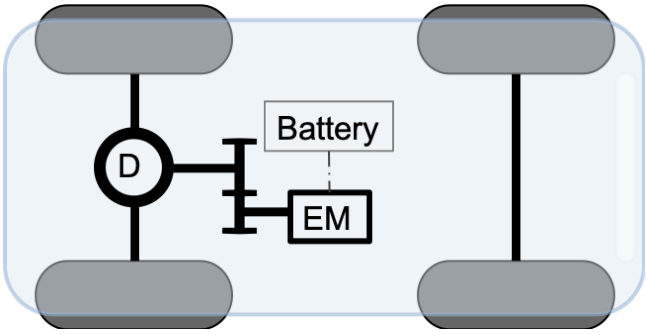

Figure 2.10: Single Motor Powertrain Topology driven at the rear axle

Figure 2.10 shows the topology of a single motor powertrain with a single-speed transmission. In this topology, the motor power transfers only through a fixed gear and a mechanical differential to reach the wheels.

Single motor topology with just one gear was recognised as an ideal option because of the wide speed range, high torque at low speeds and high efficiency over the entire operating zone when compared to a traditional ICE vehicle [19]. These features allow the powertrain to eliminate multiple gear ratios and achieve desired energy efficiency. This research paper will utilise this architecture for the majority of the simulation work.

2.5.2. Dual Motor Powertrains

A dual-motor drive is a powerful yet simple solution to improve the torque provided by the BEV. It gives improved efficiencies in the overall performance of the BEV as the torque and power requirement is distributed among the motors [26]. It also reduces the overall losses and heat dissipation from each motor.

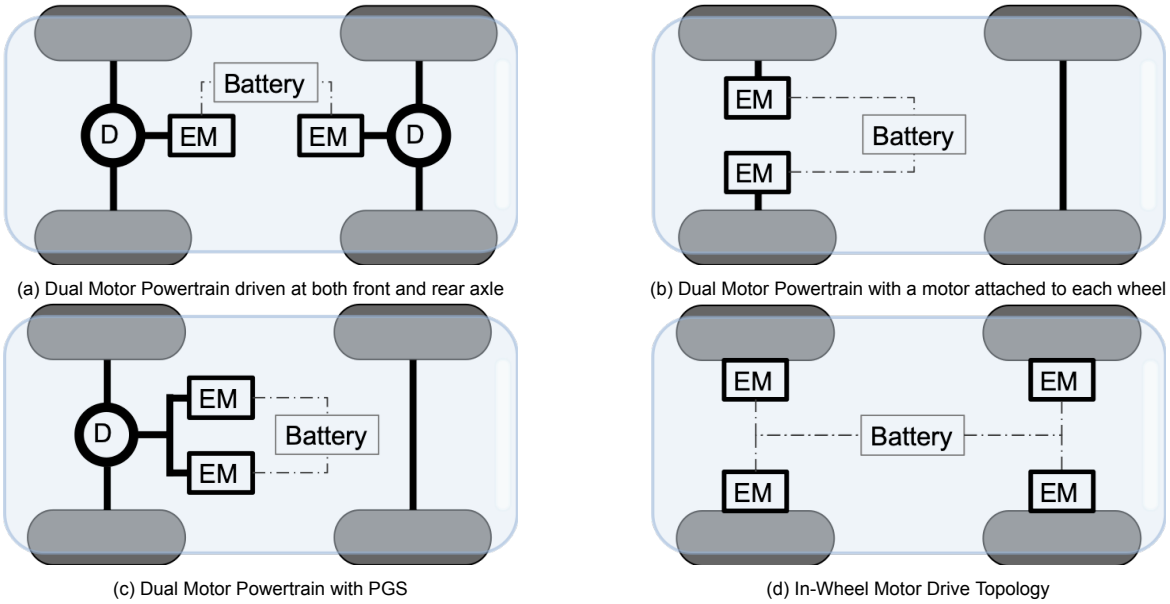

(a) Dual Motor Powertrain driven at both front and rear axle

(b) Dual Motor Powertrain with a motor attached to each wheel

(c) Dual Motor Powertrain with PGS

(d) In-Wheel Motor Drive Topology

Figure 2.11: Various Powertrain Architectures [19][25]

In this section, different advancing architectures for dual motors are covered. Figure 2.11a displays two motors mounted to front and rear axle. This architecture is popular as it allows rear-wheel drive (RWD), front-wheel drive (FWD) and all-wheel drive (AWD). These driving modes can be achieved by using appropriate control of the motors [19][27]. This also provides the advantage of imposing minimal design changes in the existing powertrain components, making it easier for implementation in the near future from a production standpoint. For this reason, this powertrain is chosen for modelling and simulation of dual motors in the heavy-duty BEV.

Figure 2.11b presents two identical motors connected to the left and right wheels of the driving axle [28]. This architecture removes the need for transmission and differential, which improves the overall powertrain efficiency. Removing the differential introduces the challenge of torque vectoring to control the yaw movement of the BEV while steering. Torque-vectoring (TV) operated via individual motor control offers advantages over active differentials such as dynamic response, maximum torque transfer and efficiency [29] [30][25]. However, to capitalise on the benefits of TV control, controllers advanced than the controllers used in today's vehicle stability control system is required [31].

Figure 2.11c showcases a torque-coupling architecture of a BEV with two motors connected to a planetary gear set (PGS). This architecture helps to utilise two different gear ratios for the two motors to propel the vehicle. This architecture is widely researched [32][33], but no production vehicle apart from GM Chevrolet Volt is found with this powertrain architecture [19].

Another powertrain architecture which is gaining popularity is the in-wheel drive seen in figure 2.11d. In this powertrain, the electric motors are placed inside the wheel with the use of a thin planetary gear set to enhance the motor torque [20]. A variant of the in-wheel drive is also being studied where the mechanical gears are entirely excluded. This arrangement simplifies the drive train and eliminates all mechanical losses. This arrangement is also called direct-drive [20]. Either variants of this powertrain has various advantages such as compact driveline, more space for the battery pack, and operation flexibility: RWD, FWD and AWD [19] [34]. However, a significant drawback observed in this powertrain is the need for motors with high torque to start and accelerate the vehicle [34]. Because of this reason, in-wheel motors have not been designed for heavy-duty vehicles. This conclusion was arrived after comparing the various manufacturers researching on in-wheel motors such as Protean Electric Ltd. [35], Elaphe propulsion technologies [36], and GEM motors [37].

2.5.3. Single Motor Powertrain with Two-Speed Transmission

Multiple-speed transmission [38] [39] are advancing in BEV powertrain designs as they can enhance the vehicle performance. With a two-speed transmission, higher torques at low speeds can be achieved to transport heavy payloads and a second gear ration can be employed to extend the vehicle top speed. Using two-speed

transmission and optimising the operating points of the motor over a given drive cycle, the energy efficiency of the BEV can be significantly improved [40]. Consequently, two optimisation problems arise the selection of the gear ratios and determination of a desirable gearshift map [41]. Though multi-speed transmission has lower transmission efficiency compared to a single-speed transmission because of the actuation system and increased mass, the variation is marginal compared to the overall powertrain efficiency [38].

The two-speed transmission is mentioned to increase the efficiency and performance of the BEV in [42] [43]. The powertrain with this transmission enables to design the driveline with an electric motor of lower peak torque. Downsizing these components in the powertrain can help reduce the manufacturing cost, driveline mass and energy consumption. Owing to these reasons, exploring this powertrain architecture is advantageous for future work. Chapter 6 explains the modelling and simulation in detail to realise the above-discussed architectures and compare the energy efficiency with the single-speed powertrain.

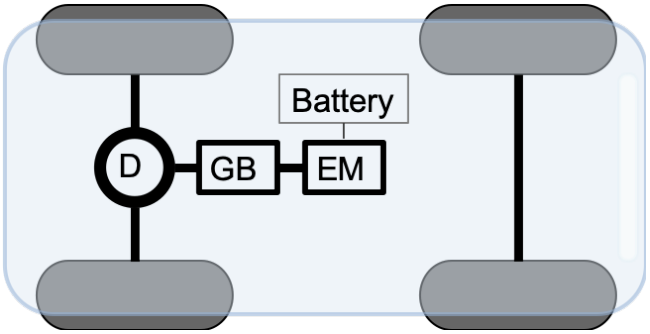

Figure 2.12: Single Motor Powertrain with Two-Speed Transmission

3

Motor Modelling

Motor modelling forms a core element in a BEV powertrain model as it is necessary to analyse the energy consumed with high accuracy. Motor efficiency maps have been an effective tool in selecting and designing the motor drive for various BEVs based on its driving profiles.

The motor modelled in this chapter is a Siemens manufactured permanent magnet synchronous motor (PMSM) from their ELFA series. The specifications of the selected motor are seen in table 3.1. Based on these values, the parameters such as maximum power, drive torque, regenerative torque, etc are used for the motor model. Further details are discussed in the latter part of the chapter.

In this chapter, the approach taken for modelling the motor to understand each of the losses during the operation of the BEV is explained. The motor losses are extracted from an efficiency map provided by the company. In the last part of the chapter, the regenerative braking control strategy implemented in the model is elaborated.

3.1. Motor Losses and Efficiency

Efficiency maps of motors are developed to obtain a clear understanding of the various losses experienced by the motor in its entire speed and torque range. The dominant motor loss components are iron loss and copper loss arising from the iron core and copper windings respectively [44].

Efficiency maps are 2D contour plots which give us information about the efficiency of operation at various values of torque and speed. The major sources of loss seen in PMSM are the same for all types of electric motors. They can be classified into four types, as follows:

3.1.1. Copper Loss

Copper losses arise due to the heating of the wires in the motor. This is due to the electrical resistance of the winding R_s which causes some of the electrical energy flowing through it to dissipate as heat. This power lost is proportional to the square of the current flowing through the three phases.

$$P = 3I^2R_s \tag{3.1}$$

We know that the motor torque is proportional to the current. However, the torque also depends on various other parameters such as the number of magnetic pole pairs, the number of turns in each coil, and other aspects of

Permanent Magnet Synchronous Motor	
Rated Voltage	650 V
Rated Current	300 A
Rated Power	200 kW @ 1500 rpm
Max. Power	240 kW
Rated Torque	2000 Nm @ 320A
Max. Torque	3800 Nm @ 600A
Max. Speed	3500 rpm
Weight	480 kg
Cooling	Water-Glycol

Table 3.1: Siemens 200kW PM Synchronous Motor Specifications

motor design [45]. Hence the copper power loss can be expressed as,

$$\text{Copper losses} = k_c T^2 \tag{3.2}$$

where k_c is a constant of proportionality which is dependent on the resistance of the winding and the magnetic flux. The fundamental copper loss can be explained as a function of d-axis current and electromagnetic torque [46]. These losses are very evident in smaller motors as they are the main contributors to losses in these machines.

Equation 3.2 is valid only in the non-flux weakening region. At high speeds, during flux weakening mode of operation, the copper loss is calculated by using the equation 3.1. The stator resistance R_s is calculated by dividing the copper loss value in the non-flux weakening region with the current value. The current calculation is explained in chapter 4. Using the calculated stator resistance and the changing current value, the copper loss in the flux-weakening region is calculated.

3.1.2. Iron Loss

Iron losses are seen in the iron parts of the motor, particularly in the rotor, due to the presence of continuously changing magnetic field. This ever-changing magnetic field can cause two types of iron losses namely, the 'hysteresis loss' and the 'eddy current loss'.

Hysteresis loss comes from the energy utilised to continually magnetise and demagnetise the iron. This is used to aligning and re-aligning the magnetic dipoles of the iron in the rotor [45]. This energy lost, even in a good magnetically soft iron, will be very small but not zero.

The second loss called the eddy current loss is observed due to the generation of current in the iron as a result of the changing magnetic field (Faraday's law). These currents flowing through the iron core of the electric motor causes heating of the iron. This loss is minimized by building a core with laminated thin sheets of iron stacked together and bolted. A layer of paint is applied on the sheets to separate it from its neighbour [45]. This increases the resistance of the iron thereby reducing the current flowing through it.

The iron losses are proportional to the frequency of the rotating magnetic field and the fundamental component of magnetic flux. The hysteresis loss increases with the frequency as frequency determines the rate at which iron is magnetised and demagnetised. Similarly, eddy currents also increase with the rate of the change of magnetic flux. Hence at higher frequencies, the hysteresis loss and eddy current loss are high. The total iron loss can be expressed using the Bertotti iron loss formula 3.3 which is the most common evaluation method used for iron loss calculation [47].

$$p_{fe} = p_h + p_e + p_{ex} = C_h B_m^2 f + C_e B_m^2 f^2 + C_{ex} f^{1.5} B_m^{1.5} \tag{3.3}$$

where p_h corresponds to the hysteresis power loss, p_e corresponds to the eddy current loss and p_{ex} corresponds to the excess loss. C_h and C_e are coefficients of hysteresis and eddy current losses. B_m is the magnitude of the magnetic flux and f is the frequency of rotational magnetic field.

In this case, the eddy current loss and hysteresis loss are simplified in terms of angular velocity of the motor. The excess loss is not included in this study as a recent study [48] shows that individual contributions of eddy current and excess loss cannot be separated. The excess loss factor is described in more detail in [49].

We know, the frequency of the rotational magnetic field is directly proportional to the rotational speed of the rotor. Hence, the eddy current and hysteresis losses can be simplified as,

$$\text{Eddy Current losses} = k_{ed}\omega^2 \tag{3.4}$$

$$\text{Hysteresis losses} = k_h\omega \tag{3.5}$$

where k_{ed} and k_h are proportionality constants. In reality, k_{ed} and k_h are not actually constants but they are dependent on the strength of the magnetic field and other non-constant factors. The fundamental iron loss can be explained as a function of rotational speed and both d-xis and q-axis currents [46]. It is also found that iron losses can vary with non-sinusoidal field arising from various PWM techniques that may be implemented [44]. In PMSM, the iron loss values are not as varying as other motors such as separately excited DC motors [45].

3.1.3. Friction and Windage Loss

The friction loss is the loss due to the friction in the bearings of the motor. The friction torque that contributes to this loss is generally a constant value and usually negligible. The windage loss is due to the wind resistance experienced by the rotor. The wind resistance forced usually increases with the square of the speed.
The power loss from these two resistive torques is calculated by multiplying with the angular velocity and hence the following is obtained,

$$\text{Friction loss} = T_f\omega \tag{3.6}$$

$$\text{Windage loss} = k_w \omega^3 \tag{3.7}$$

Here, T_f is the friction torque and k_w is constant which is obtained from the size and shape of the motor and is also dependant on the presence of a cooling fan.

3.1.4. Constant Loss

Constant losses are the losses in the motor even when the motor is stationary. These losses are independent of torque or speed of the motor. They arise as an effect due to the operation of power electronics at all time [45]. These losses also known as additional losses are related to the high frequency harmonics from the inverters. This loss can be represented with the letter C. Combining all the losses described above, the total loss equation can be written as follows.

$$\text{Total losses} = k_c T^2 + k_{ed} \omega^2 + k_h \omega + T_f \omega + k_w \omega^3 + C \tag{3.8}$$

Here, since both the hysteresis loss and the friction loss are proportional to the angular speed, they can be combined into one term for modelling. Also, as the inverter losses are taken into account and separately calculated, the constant loss C is neglected. Hence the above equation can be rewritten as

$$\text{Total losses} = k_c T^2 + k_h \omega + k_{ed} \omega^2 + k_w \omega^3 \tag{3.9}$$

3.1.5. Efficiency

The efficiency of the motor is the ratio of the output power by the input power and the input power in case of a motor is the sum of output power and its losses.

$$\eta_m = \frac{\text{output power}}{\text{input power}} = \frac{\text{output power}}{\text{output power} + \text{total losses}}$$

$$\eta_m = \frac{T\omega}{T\omega + k_c T^2 + k_h \omega + k_{ed} \omega^2 + k_w \omega^3} \tag{3.10}$$

This equation will give us an estimate of the efficiency of the motor used in the BEV and help us draw efficiency maps. These maps give us an insight into the motor performance when used in the powertrain of the medium-duty or heavy-duty BEVs. Such information can be used further in future works for motor design to improve the efficiency by precisely identifying the loss contributing factors in a motor. The loss constants in this efficiency equation are determined from experiments or by regression using measured values of efficiency [45].

When the motor runs as a generator during regenerative braking, the input power is provided by the rotor of the PMSM. The output power is the electrical energy which flows through the inverter and recharges the battery. As both the input and output power is different during braking, the generator efficiency (η_g) formula becomes -

$$\eta_g = \frac{\text{output power}}{\text{input power}} = \frac{\text{output power} - \text{total losses}}{\text{input power}}$$

$$\eta_g = \frac{T\omega - (k_c T^2 + k_h \omega + k_{ed} \omega^2 + k_w \omega^3)}{T\omega} \tag{3.11}$$

3.2. Calculation of Loss Constants

The efficiency map is built using the above formula with only torque and speed values. The loss constants are unknown and needs to be identified. Hence, arbitrary values are taken as used in [45] as a point of reference. This helps in estimating a range of values for each loss constant.

A reference efficiency map of the electrical motor drive (motor + inverter) used in DAF CF Electric is obtained from the department of DAF Product Development. This efficiency map, taken as the reference map, is matched with the efficiency map that is built using the above efficiency formula. In order to obtain an efficiency map closer to the actual map and to estimate the motor losses accurately, two algorithms were experimented.

In the first method, an iterative approach was taken in which a MATLAB script is used to iterate over a range of all possible loss constant values and compare the plots. In the second method, an evolutionary algorithm based optimization method was used called the particle swarm optimization (PSO) method to obtain the loss constants with minimal computational requirement. The following sections explain the two algorithms in detail.

3.2.1. Iterative Algorithm

In this algorithm, a straightforward approch is taken to calculate the efficiency map by plugging in different values for the loss constant. Firstly, two arrays are defined for torque and speed based on the operating range of the motor. Using these arrays, a matrix is built containing the product of the torque and speed which corresponds to the output power.

Four variables are then initialised for copper loss constant (k_c), eddy current loss constant (k_{ed}), hysteresis loss constant (k_h) and windage loss constant (k_w). Using equation 3.10, the efficiency of the motor at different values of torque and speed are calculated and stored into a resultant matrix. However, it is to be noted that the reference efficiency map is the combined efficiency of the motor and the inverter. Hence, the inverter efficiency is calculated as explained in chapter 4 and it is combined with the motor efficiency map by multiplying the two matrices. The values of this product matrix at locations where the output power exceeds the motor's maximum output power, i.e. 240kW, is forced to zero.

The accuracy of match between this calculated product matrix and the reference matrix is then estimated by performing an element-wise comparison and ensuring that the difference in efficiency is below 0.5%. The accuracy of these maps to the reference map is estimated in each iteration with different values of k_c, k_h, k_{ed} and k_w.

Running the script for various ranges of the loss constant values, the maximum achievable accuracy is estimated. The k_c, k_h, k_{ed} and k_w constants, for which maximum accuracy is achieved, are chosen for the final efficiency map. The chosen loss constant values are as follows:

$$k_c = 0.0018$$

$$k_h = 14$$

$$k_{ed} = 0.0036$$

$$k_w = 1.8 \times 10^{-5}$$

It is found that a resultant efficiency plot has a 71.5% perfect match with the reference efficiency plot. This number is only a measure based on the difference between the two maps. This is further explained in section 3.3. This means that the motor losses obtained from the model are close to the actual losses experienced by the motor during operation.

3.2.2. Particle Swarm Optimization (PSO)

Particle Swarm Optimization (also known as PSO) is a simple yet very powerful optimization algorithm which utilises only primitive mathematical operators making it computationally faster without much memory requirement [50]. For the same reason, this algorithm is being successfully applied in various fields such as machine learning, image processing, data mining, etc.

A PSO algorithm has a population (called swarm) of candidate solution (called particles). This computational method tries to improve the candidate solution by continuously moving the particles in a search space according to few mathematical formulae which helps determine its new position and velocity in the search space [51].

Working of PSO

The working of the particle swarm optimisation technique explained in this section, is also represented in a flowchart in figure 3.1 for clear understanding. In this optimisation technique, a swarm of candidate solutions is positioned arbitrarily in a search space. The search space is a set of all possible solutions for the optimization problem. In this case, the optimization problem is to maximize the match between the efficiency map plotted using the loss constants and the reference efficiency map. The swarm is the four loss constants of the motor and all possible solution for these loss constants make up the search space.

Let a vector $x_i(t)$ denote the position of particle i in time step t. Here, $x_1(t)$ will represent k_c, $x_2(t)$ will represent k_h, $x_3(t)$ will represent k_ed and $x_4(t)$ will represent k_w. Each of the particle will have a velocity associated to it along with its position denoted by $v_i(t)$. Velocity defines the movement of the particle in the search space which includes direction, distance and step size. In this technique, the particles interact with each other to find the best solution.

By defining the mathematical model of the motion of the particle in PSO, an optimisation tool is developed to find the optimal candidate solution. In addition to the position and velocity of the particle, a memory element is also introduced to save its own best position (personal best, $pbest$). Along with $pbest$, another memory element is added to record the common best position of the whole swarm which is denoted as global best ($gbest$).

The mathematical model is defined by simply updating the position and velocity of each of the particle. The direction in which the particle is made to move is a vector sum of three vectors: the vector parallel to the

previous velocity of the particle, the vector parallel to the direction to the personal best and the vector parallel to the direction of the global best. Thus the particle is made to move to a new position which is probably a better location as it utilises the information of both $pbest$ and $gbest$.

The mathematical model of motion of PSO can be described as follows. One of the equations that is simpler is the equation for updating the position of the particle and it can be described as

$$x_i(t+1) = x_i(t) + v_i(t+1) \tag{3.12}$$

where,

$v_i(t+1)$ is the new velocity vector.

The equation for updating the velocity vector is given by equation 3.13.

$$v_i(t+1) = wv_i(t) + r_1c_1\,(pbest_i(t) + x_i(t)) + r_2c_2\,(gbest(t) - x_i(t)) \tag{3.13}$$

where,

w is the inertia coefficient

r_1 and r_2 are uniformly distributed numbers in the range of 0-1

c_1 and c_2 are acceleration coefficient

wv_i is the inertia term,

$r_1c_1\,(pbest_i(t) + x_i(t))$ is know as the cognitive component and

$r_2c_2\,(gbest(t) - x_i(t))$ is known as the social component.

Inertia term, cognitive component and the social component combined gives the new velocity vector. All the particles in the swarm are garunteed to follows these two equations.

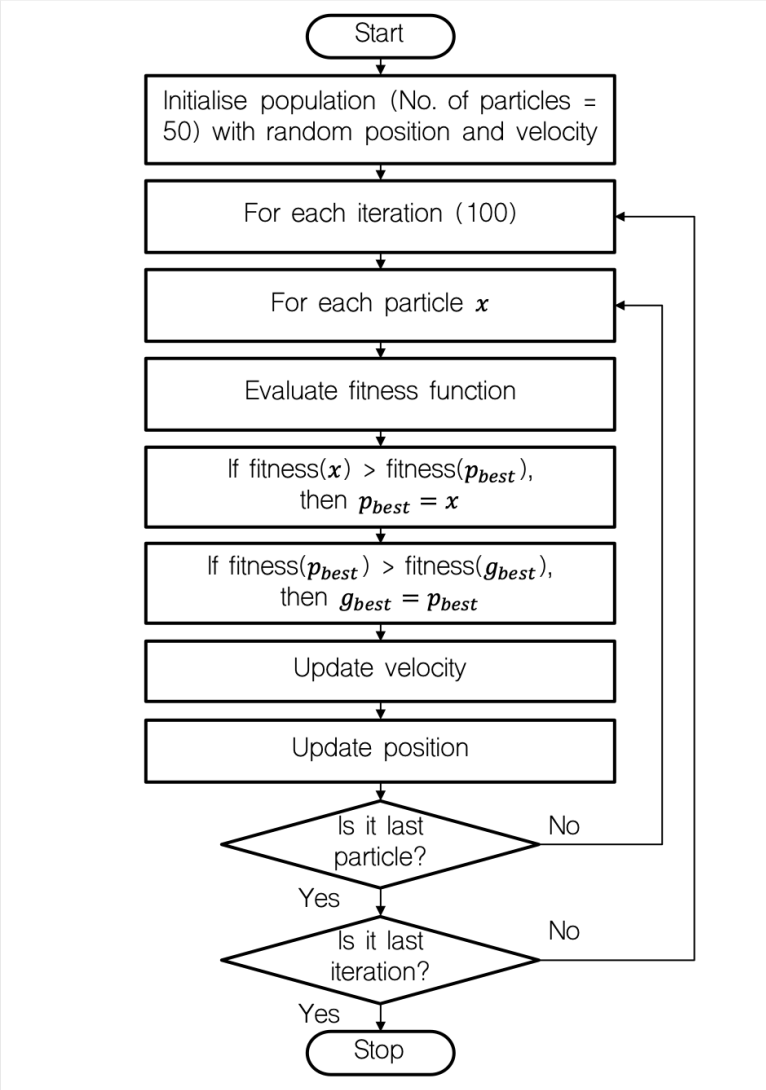

Figure 3.1: Flowchart of PSO Algorithm [52]

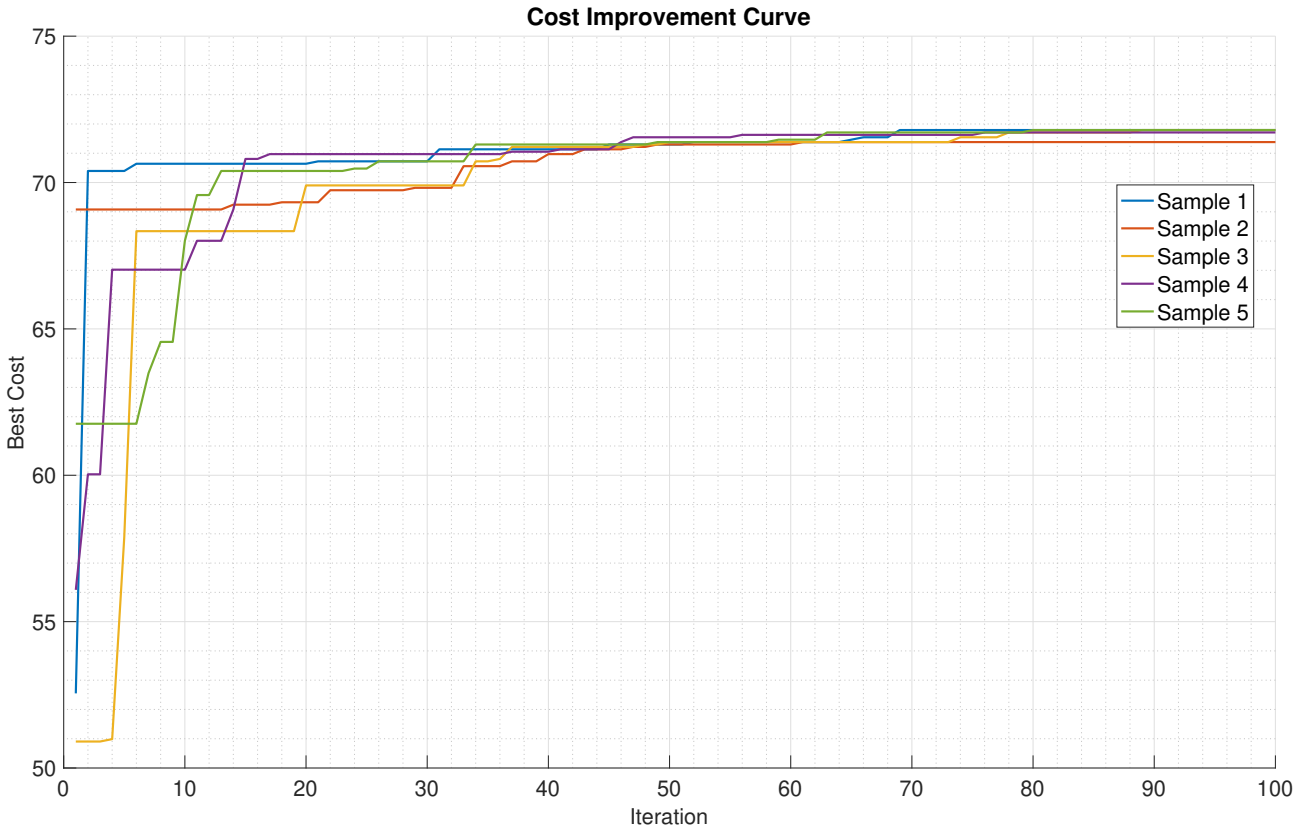

Figure 3.2: Cost Improvement Curve for 5 sample runs of PSO Algorithm

PSO Results

The program written to implement the particle swarm optimisation has a total of 100 iterations with a swarm size of 50 particles. Upon execution, the particles are randomly positioned and the cost function is calculated for each iteration. Depending on the number of iteration, the swarm converges to the most optimum cost function.

To observe the randomness of the initialisation and convergence of solution, the program is repeatedly run for 5 times. Each of the run will be refered to as sample. For each sample, a graph of cost value vs iteration is plotted. The figure 3.2 show the cost improvement curve for the five sample runs of the code. It can be observed that the initial value of cost is scattered and random in each sample run. Towards the end of the iteration, the cost values converge to a common optimised value.

The closeness of the resultant efficiency plot to that of the reference efficiency plot is about 71.79% with a maximum permissible error of only 0.5%. Thus, the accuracy of both the algorithm is approximately the same. However, a major difference is seen in the computational time. This algorithm reduces the run time drastically. The iterative algorithm computes the loss constants in the range of 8-10 mins. Whereas, PSO algorithm requires less than a mins. Hence, PSO algorithm is advantageous for this application. The final values of each of the loss constants are selected based on the sample with the highest best cost value. The results obtained are as follows:

$$k_c = 0.001882$$

$$k_h = 14.7255$$

$$k_{ed} = 0.003641$$

$$k_w = 1.7761 \times 10^{-5}$$

3.3. Motor Efficiency Map

With the results from the MATLAB script, the motor efficiency map is plotted against torque and speed of the motor as seen in figure 3.3. The values of torque and speed that produce higher efficiencies are highlighted in yellow and lower efficiencies tend towards the blue spectrum.

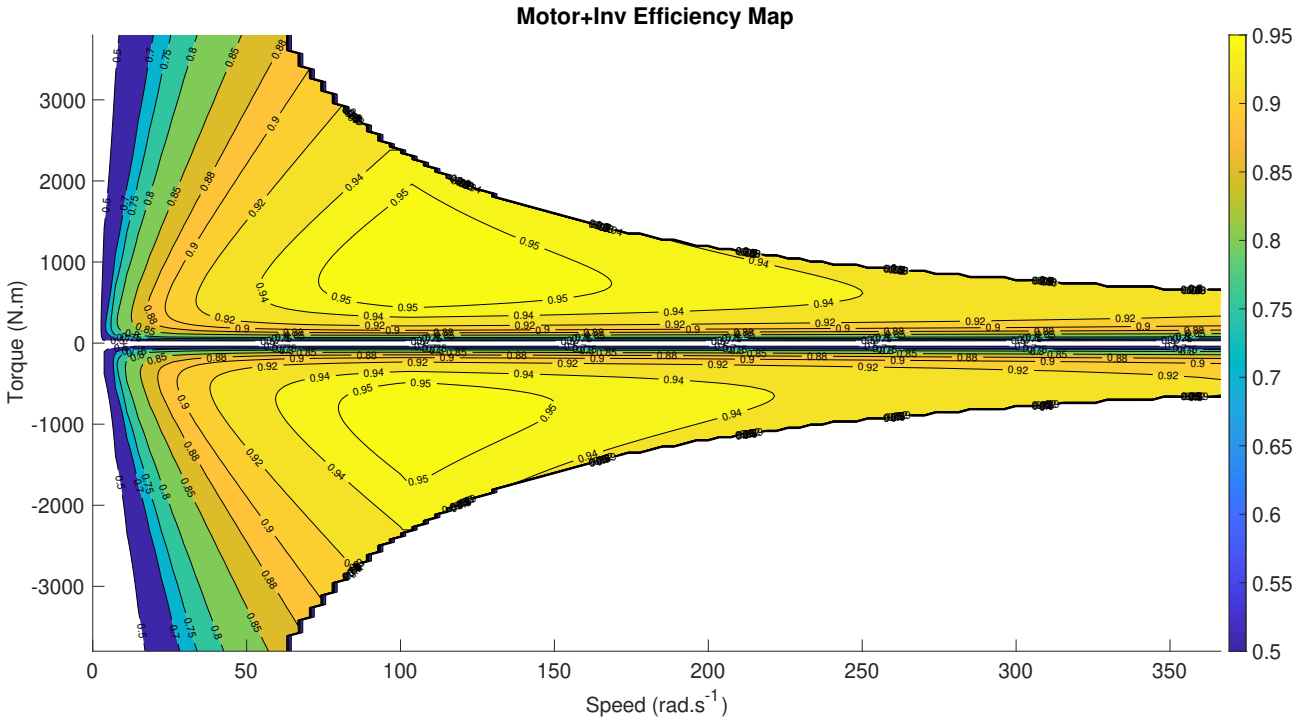

Figure 3.3: Calculated Efficiency Map of the ELFA motor used in the powertrain

For further insight into the accuracy of the plot obtained, an error map is plotted by calculating the difference between the reference efficiency curve and the calculated efficiency curve. This contour plot, as shown in figure 3.4 gives insight into locations at which the estimated losses will not be equal to real world. From figure 3.4, we can see that the accuracy is poor only at very low speed and low torque region. This can be explained due to the fact that the loss constants exhibit more variations and this non linearity cannot be addressed by the simplified efficiency equation used. Finite element analysis will help obtain result address this issue. Unfortunately, sufficient information about the motor was not available to execute this analysis.

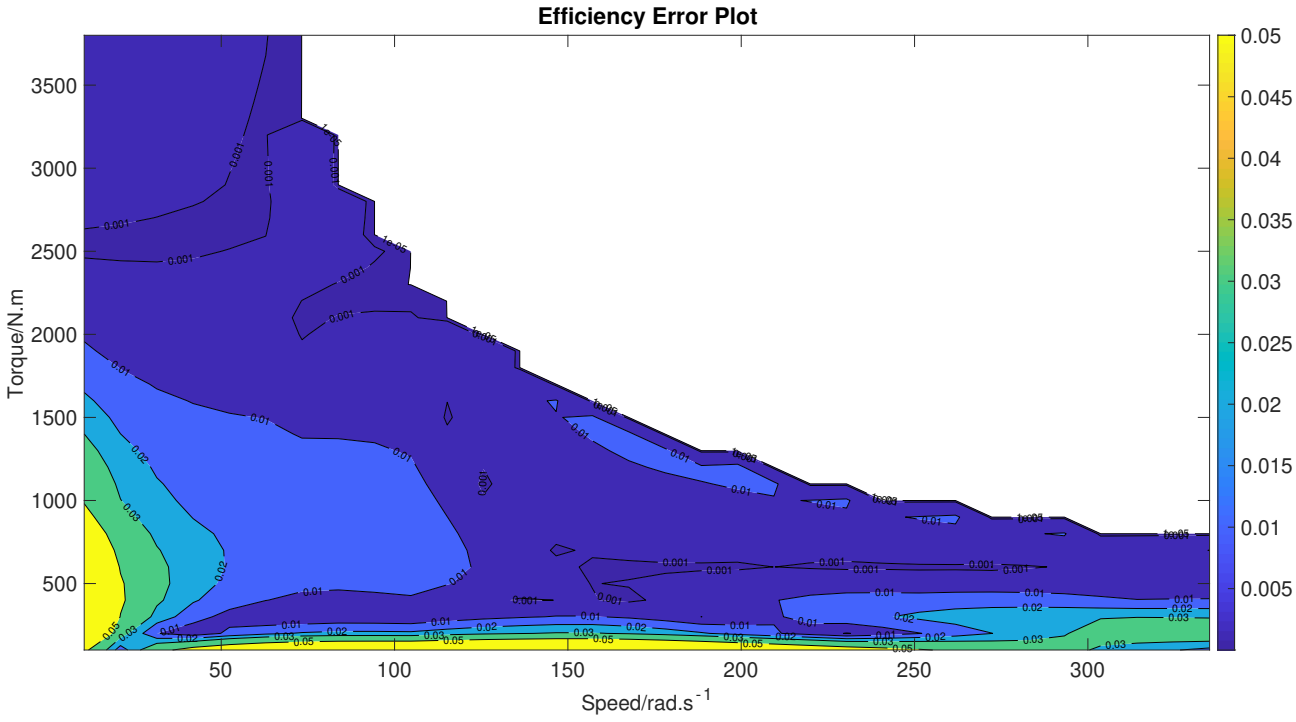

Figure 3.4: Curve showcasing the difference in the calculated efficiency map and the reference efficiency map

Figure 3.5 shows the motor efficiency map along with the points of motor operation at different torque and

speed values in one drive cycle. This gives information on the most frequently operated efficiency regions in one driving cycle. The driving cycle considered here is the real-world drive cycle data obtained from the company's field test results. Such plots can be useful during the selection of motors for different trucks based on their operation. For example, a groceries distribution truck and a garbage collection truck will have different driving cycles and that gives different operating points in their corresponding drive cycles of operation. Various medium-duty and heavy-duty BEVs are used for various purposes and on the grounds of optimising their performance, such approaches can be taken in the design phase provided motor efficiency curves are available.

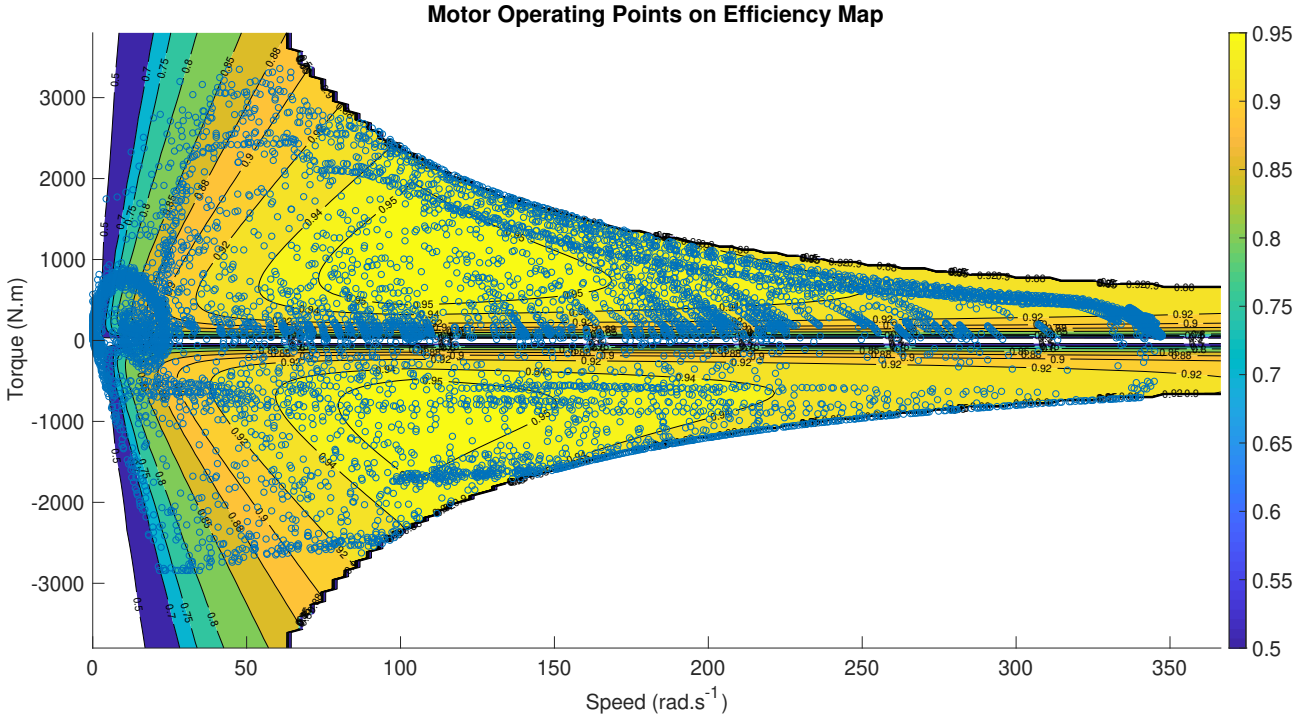

Figure 3.5: Efficiency map including the motor operating points in company provided drive cycle

3.4. Regenerative Braking

Regenerative braking is one of the key features of an electric vehicle that determines the range of the vehicle. In medium and heavy-duty vehicles, due to the larger inertia, the kinetic energy of these vehicles is very large. The kinetic energy that is dissipated during braking can be recovered in an electric vehicle due to the motor's inherent ability of regeneration. The cooperation of the frictional brakes and the regenerative brakes is called torque/brake blending and it is an important aspect in EV design to eliminate driveline disturbances [53]. The regenerative torque is calculated using the formula,

$$T_{regen} = \frac{P_{gen}}{\omega} \tag{3.14}$$

where, P_{gen} is the maximum power the motor is able to generate in generator mode and ω is the angular velocity in rps. After calculation of T_{regen}, the serial braking strategy is followed to perform brake blending.

3.5. Brake Blending

There are two kinds of braking strategies used to implement brake blending and they are serial and parallel braking strategy. The difference between the two types is studied in [54] and the following conclusion is made. Parallel braking strategy, seen in the left side of figure 3.6, is a simple braking strategy where the brake force, when brakes are applied, is distributed uniformly between the friction brakes and regenerative brakes.

Whereas, the serial regenerative braking strategy (right side of figure 3.6) is implemented in such a way that when the brakes are applied, the total brake force is first sent to the regenerative brakes and only when excess brake force is demanded, friction brakes are applied. Even in frictional braking, brake at the non-drive axle is applied first before the drive axle brake is applied. The yellow colour represents the regenerative area while the red coloured area represents the brake force split between the friction brakes depending on the brake pedal input.

Using this strategy, the fuel efficiency can be increased by 15-30% [54]. This gives maximum utilisation of the regenerative brakes. The small yellow portion at the bottom, in figure 3.6, which reads compression regen refers to regeneration when accelerator pedal is released and the truck coasts in the absence of brake pedal input.

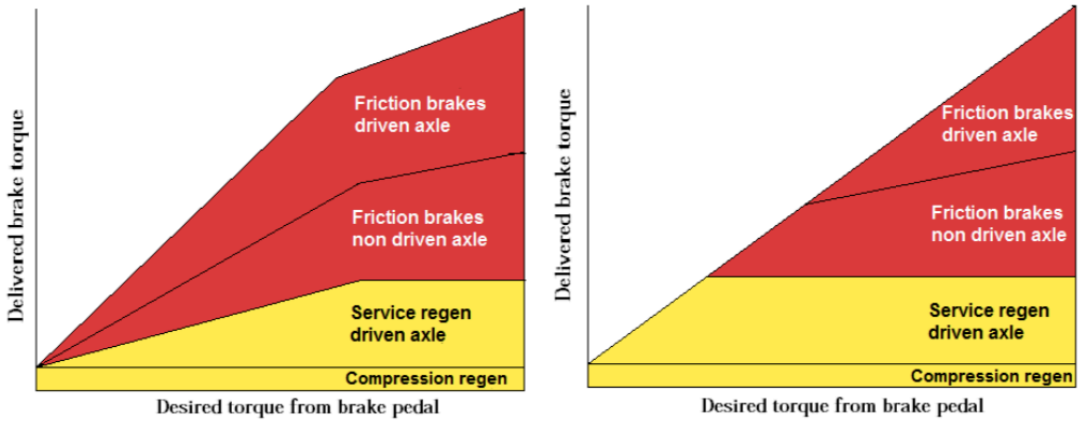

Figure 3.6: Comparison of Parallel and Serial Braking Strategy [54]

The BEV is driven at the rear wheels which means the motor is attached to the rear wheels. This implies that maximum kinetic energy should be retrieved from the rear wheels during braking. In this model, the braking torque is divided between the front and rear wheels in a ratio of 30:70. This fraction is taken as an assumption for brake force distribution [54].

3.5.1. Maximum Braking Force

A PI controller is used to determine the amount of drive torque and brake torque that is required to make the truck follow the reference speed profile. These signals are taken as the input from acceleration pedal and a brake pedal. The acceleration pedal is fed as an input to the motor and the brake pedal value is used to calculate the amount of the brake force that is to be distributed between the motor and the friction brakes.

The maximum brake force is calculated based on the equation 3.15 as seen in [55]. This value is multiplied with the percentage of the brake pedal signal that is applied to get the required brake force. This brake force is then distributed between the regenerative brake and frictional brakes using the serial regenerative brake blending strategy.

$$\text{Maximum braking force, } F_{b,max} = C_r M_{truck} g \tag{3.15}$$

where,

C_r is the coefficient of friction, M_{truck} is the mass of the truck and g is the acceleration due to gravity.

3.5.2. Serial Regenerative Braking Strategy

The distribution of the braking forces in serial braking is executed as shown in the flowchart 3.7. Firstly, the state-of-charge (SoC) is checked if it is lesser than 90% and if not, then the battery is not recharged via regenerative braking to prevent degradation of the battery. Recharging the battery at high voltages can affect the ageing of the battery.

This SoC limit is usually selected after testing as there is a trade-off between vehicle range and battery life. Using regenerative braking in the entire range of SoC can help improve the range of the vehicle but degrades the battery faster. The normal operating range of SoC in an electric truck is usually taken as 10-90%.

If SoC is less than the maximum recharging limit of 90%, then it is checked if the entire braking forced required can be given by regenerative braking. If that is the case, then the entire braking force is provided by the regenerative braking in the front wheels. If not, it is checked if 70% of the required braking force can be provided by regenerative braking. If yes, then 70% of the total braking is provided by the regenerative braking in the rear wheels and remaining 30% is provided by the front friction brakes. If none of the conditions is satisfied then the extra braking forces required in rear wheels apart from the regenerative braking is provided by rear friction brakes and 30% of the total braking is provided by the front friction brakes.

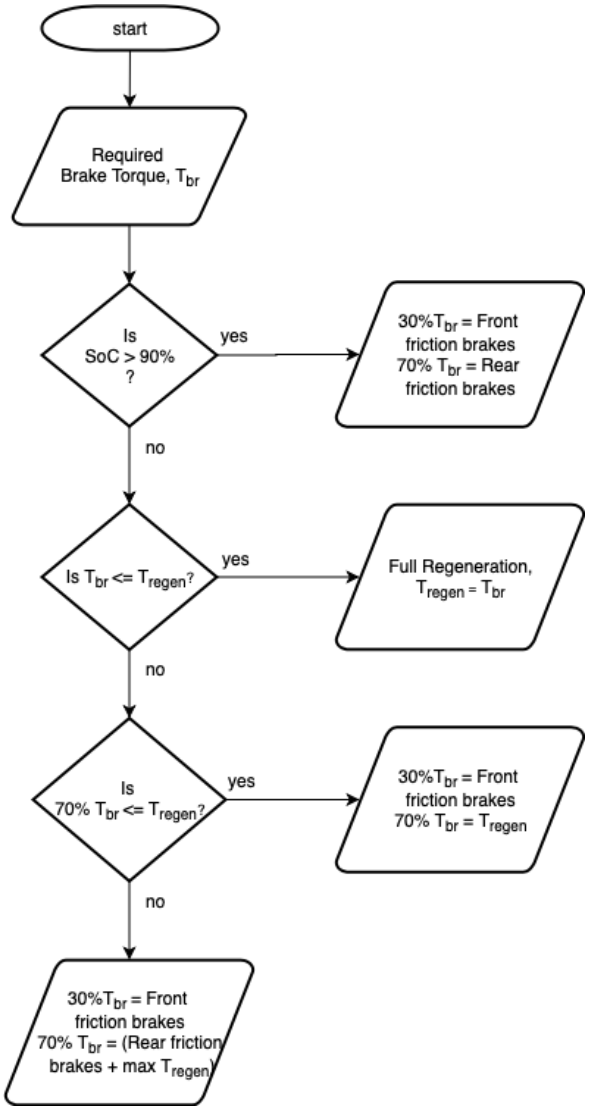

Figure 3.7: Serial regenerative braking flowchart [54]

Another important condition is also taken in the regenerative braking strategy. When the speed is less than 5 km/h, the regenerative braking is not utilised for two reasons. One is that at low motor speeds, the electromotive force that is generated is very low leading to charging of cells at low voltages and high currents [20]. Secondly, at low speeds, the charging and discharging cycles are very short. This leads to the phenomenon of 'micro-cycling' which arises due to the continuous change of direction of the high currents and this affects the lifetime of the battery pack [56].

4

Inverter Modelling

Power electronic inverters form a fundamental part in the propulsion system converting the DC power flowing from the battery to AC power for motor operation. During this conversion, some amount of power is lost at the semiconductor switches which enable this conversion. The inverter model comes in-between the motor model and the battery. The output signal from this model is the power drawn by the battery and this will help in using this model for testing the battery packs in future.

In this chapter, the following approach is taken to model the inverter losses. Firstly, an ideal inverter topology suitable for the heavy-duty BEV application is chosen and the power electronic switch used is selected. Secondly, the approach taken to calculate the inverter losses is discussed. Finally, the efficiency map and various losses are plotted for the designed powertrain model.

4.1. Inverter Topology

The most widely used inverter topology for all the battery electric vehicle (BEV) application is 2-level 3-phase inverters. As the powertrain of the medium-duty/heavy-duty BEV runs on high voltage, these inverters are designed with IGBT switches. This is mainly because IGBTs are more capable of handling higher voltages than MOSFETs [24]. All the commercially used inverters in large BEVs use IGBT switches for their application.

An inverter model is added in the powertrain to analyse the losses experienced by the semiconductor switching devices on a system level. The two main losses experienced by these power devices are conduction losses and switching losses.

As the Siemens ELFA system motor drive is chosen, the inverter used in this system is to be modelled. Some information that is available of the inverter are the input DC voltage rating, rated and maximum current and power values, and the switching frequency. The inverter specification is not showcased here due to confidentiality reasons. Based on the rating, the IGBT switch and diode is to be selected. The pulse width modulation (PWM) scheme used in this system is also unknown. Hence, for simplicity, sinusoidal PWM is assumed.

4.2. Switch Selection

Considering the application and the available specification of the inverter, an IGBT and freewheeling diode is selected that is most compatible with the ratings of the actual Siemens ELFA inverter. Semikron International had collaborated with Siemens to provide the semiconductor switches to build their motor drive systems [57]. Based on this collaboration, various Semikron International power devices were compared to select the most compatible IGBT module comprising of both an IGBT switch and a reverse recovery diode.

The peak voltage and current rating of the IGBT module are selected based on the maximum dc voltage $V_{d,max}$ and the maximum output current $I_{o,max}$ at maximum loading [58]. The output current $I_{o,max}$ is considered to be purely sinusoidal wave as the motor windings have large inductance. Therefore, each IGBT module would be desired to have the following rating:

$$V_T = V_{d,max} \tag{4.1}$$

$$I_T = \sqrt{2} I_{o,max} \tag{4.2}$$

where $V_{d,max}$ is the DC bus voltage, and $I_{o,max}$ is the rms value of the maximum inverter output current. The IGBT voltage rating is chosen to be above 900V as the DC voltage level is 650V. A margin is maintained in the case of increased battery voltages during braking or IGBT turn-off voltage peaks [58]. Also, when the battery

is fully charged, the voltage of the battery is slightly >750V. From the above equation, the current rating of the switch can be taken as 600A.

The SEMIKRON SKiM600GD126DLM IGBT module is selected for this application as it fits perfectly with the required specifications of voltage and current [59]. As per the information from the datasheet, this IGBT module is typically used for three-phase inverters for AC motor speed control. The frequency of the inverter operation is taken to be 6 kHz from the frequency range mentioned in the inverter datasheet. For the calculation of the total energy lost from each IGBT module during the operation, various parameters are required and the values of these parameters can be extracted from the datasheet of the IGBT module.

A more promising technology is arising in which the IGBT switches are built using SiC semiconductor material. It claims to decrease the losses by more than 2 times [60]. However, they are not actively used in commercially available high voltage applications. SiC MOSFETs are currently gaining traction in various electric vehicle inverters [61].

4.3. Inverter Loss Calculation

The conduction and switching losses of both IGBT and diode are modelled as in [62] with the assumption of ideal sinusoidal PMW three-phase voltage. This is then further scaled to estimate the total inverter losses and efficiency.

Losses in the driver circuit and parasitic inductance or capacitance are assumed to be negligible. On-state, turn-on and turn-off losses are considered for IGBTs and the on-state and turn-off (reverse recovery) losses are considered for diodes. The reverse blocking losses of the IGBTs and the turn-on losses of the diodes are assumed to be negligible. The diodes are assumed to have a fast diode turn-on process and hence the turn-on losses are neglected in the following method.

It is to be noted that parameters such as junction temperatures, load current and duty cycle vary with respect to the fundamental frequency of the AC signal (e.g. 50/60 Hz) [62]. Owing to this, the switching losses and on-state power dissipation of IGBT and diode are not constant. For precise results, in-depth analysis of system losses will be required. In this analysis, the following assumptions are made

- IGBT and diode switching times are neglected
- Junction temperatures are assumed to constant throughout the operation
- Linear modulation
- Switching ripples of the AC current signal is neglected

4.3.1. Conduction losses

Conduction losses occur during static operation of the switches. The power electronic components can be modelled by their forward characterization neglecting the dynamics. It is modelled as a function of constant voltage drop and on-state resistance in a linear fashion [62]. This gives a good representation of the switch's forward characterization.

$$P_{ds} = V_{ds} i_{ds} + R_{on} i_{ds}^2 \tag{4.3}$$

where P_{ds} is the power drop between the drain and source of the switch, V_{ds} is the voltage drop between drain and source, i_{ds} is the current flowing through the drain and source and R_{on} is the on-state resistance.

In PWM inverters, the inverter conduction losses depend on the duty cycle which is further dependent on the modulation index (m_a), phase delay (ϕ) and electrical angle (θ) also. The duty-cycle D of a pulse of a sinusoidal PWM signal is calculated as follows (D=1 when D≥1) [63]

$$D = \frac{1}{2}\left(1 + m_a sin(\theta - \phi)\right) \tag{4.4}$$

Each phase of the inverter has sinusoidal current and voltage signals flowing through it. Hence, the conduction loss can be calculated by finding the product of these signals and duty cycle over a phase period (0-π) for one cycle (2π).

$$P_{\text{conduction, IGBT}} = \frac{1}{2\pi}\int_0^{\pi} \left(I_{CP} sin\theta \times V_{CE(sat)} sin\theta \times D\right) d\theta \tag{4.5}$$

$$P_{\text{conduction, IGBT}} = \frac{1}{2\pi}\int_0^{\pi} \left(I_{CP} sin\theta \times V_{CE(sat)} sin\theta \times \frac{1}{2}\left(1 + m_a sin(\theta - \phi)\right)\right) d\theta$$

where I_{CP} is the peak collector current and $V_{CE(sat)}$ is the collector-emitter saturation voltage. The peak collector current is the same as the peak value of the AC phase current and the collector-emitter saturation voltage is equal to the on-state threshold voltage [63].

Simplifying the above the equation, the average on-state loss of an IGBT can be written as

$$P_{\text{conduction, IGBT}} = \left(\frac{1}{2\pi} + \frac{m_a cos(\phi)}{8}\right) V_{th} I_m + \left(\frac{1}{8} + \frac{m_a cos(\phi)}{3\pi}\right) R_{on} I_m^2 \tag{4.6}$$

where V_{th} is the on-state threshold voltage, I_m is the peak value of the AC phase current and R_{on} is the on-state resistance. Both V_{th} and R_{on} are dependent on temperature [64].

The freewheeling diode loss model can be represented as follows

$$P_f = V_{f0} i_f + R_{on} i_f^2 \tag{4.7}$$

where V_{f0} is the constant voltage drop of diode, i_f is the current flowing through the freewheeling diode and R_{on} is the on-state resistance of the diode. The forward conduction loss of freewheeling diode is calculated is the same way. The duty cycle of a pulse of a PWM signal given by (D=0 when $D \leq 0$)

$$D = \frac{1}{2}\left(1 - m_a sin(\theta - \phi)\right) \tag{4.8}$$

Similar to the conduction losses of the IGBT, the diode conduction loss equation can be calculated and simplified as

$$P_{\text{conduction, diode}} = \left(\frac{1}{2\pi} - \frac{m_a cos(\phi)}{8}\right) V_{th} I_m + \left(\frac{1}{8} - \frac{m_a cos(\phi)}{3\pi}\right) R_{on} I_m^2 \tag{4.9}$$

The combined conduction losses contributed by the IGBT and diode in the IGBT module can be written as,

$$P_{cond} = P_{\text{conduction, diode}} + P_{\text{conduction, IGBT}} \tag{4.10}$$

4.3.2. Switching losses

The equation 4.11 can be used to estimate the average turn-on and turn-off switching losses per switching period [65] [62].

$$P_{sw} = f_{sw} \times E_{on+off} \frac{\sqrt{2}}{\pi} \times \left(\frac{I_m}{\sqrt{2} I_{ref}}\right)^{K_i} \times \left(\frac{V_{DC}}{V_{ref}}\right)^{K_v} . \left(1 + TC_{sw} . \left(T_j - T_{ref}\right)\right) \tag{4.11}$$

where f_{sw} is the switching frequency, K_i and K_v are the current and voltage dependencies of switching loss respectively, I_m is the amplitude of the inverter current, V_{DC} is the DC voltage and V_{ref} and I_{ref} are the reference DC voltage and DC current respectively to which the energy lost correlates. TC_{sw} is the temperature coefficient for switching losses (~0.003 1/K for IGBT and ~0.006 1/K for diode), T_j is the junction temperature and T_{ref} is the reference value of temperature from the datasheet.

In this test, T_j and T_{ref} are assumed to be the same. Hence the temperature component is neglected. The V_{ref} and I_{ref} are taken from the datasheet of the IGBT module. The current and voltage dependency values are chosen as follows for IGBT and diode. For IGBT, $K_i = 1$ and $K_v = 1.35$ and for diode, $K_i = K_v = 0.6$ [65][62].

The energy lost during turn-on and turn-off $E_{on,off}$ of IGBT and reverse recovery E_{rr} energy of diode are taken from the datasheet for the loss calculation. However, they are not constant throughout the operation of the inverter but are dependent on four factors [62]:

- the rate of rise of commutation current di/dt or gate resistance (R_G) of IGBT
- the DC link voltage (V_{DC})
- the forward current (I_m)
- the junction temperature (T_j)

In the datasheet, the energy lost vs R_G and energy lost vs I_m is provided in graphs which can also be used for switching loss calculation. The table 4.1 provides the relation of the energy loss with respect to collector current obtained using the curve fitting tools.

Collector Current I_m (A)	100	200	300	400	500	600
Turn-on energy E_{on} (mJ)	10	18	25	35	42	52
Turn-off energy E_{off} (mJ)	15	26	40	54	68	80
Reverse recovery energy E_{rr} (mJ)	8	12	18	20	22	23

Table 4.1: Data extracted from the datasheet of the IGBT module indicating the relation between turn-on, turn-off and reverse recovery energy with respect to the collector current

Switching losses will also be contributed by gate pulses, a gate driver circuit and the commutation inductance [65]. However, these aspects are considered negligible due to lack of information. Therefore, the IGBT turn-on and turn-off switching losses along with the diode's switching losses are individually calculated using equation 4.11. All the losses are added to estimate the total switching loss contributed by the IGBT module as a whole.

$$P_{sw} = P_{\text{sw, IGBT (on)}} + P_{\text{sw, IGBT (off)}} + P_{\text{sw, diode}} \tag{4.12}$$

The losses experienced by the power devices is modelled on only one module. As the inverter operation is symmetrical, this is scaled to the other modules by multiplying with the number of modules as [64]. The total power lost at the inverter P_{inv} is given by the equation

$$P_{inv} = 6 \times (P_{cond} + P_{sw}) \tag{4.13}$$

Furthermore, after substituting the on-state threshold voltage and resistance in the conduction equation, the value of the AC phase current is to be calculated. The conduction losses are mainly contributed by the current flowing through the switch and the switching loss is influenced by the frequency of the switching operation.

4.4. Current Calculation

The calculation of phase current is split into two parts as the current is not constant over the entire speed range. The permanent magnet synchronous motor is controlled by using field-oriented control (FOC) technique to achieve a wide speed range for traction application. There are two modes of control that is implemented in FOC technique. They are

- $I_d = 0$ control at low speeds
- Field weakening control at high speeds

4.4.1. $I_d = 0$ Control

This control technique is performed to maintain the maximum current in the quadrature axis (q-axis) of the motor to achieve Maximum Torque per Ampere (MTPA). The current along the direct axis (d-axis) is maintained at zero to push all the current in the q-axis and hence the name.

The FOC technique is implemented by transferring the three-phase varying currents in the stator frame to dq synchronously rotating frame. This is achieved using the Clarke and Park transform. The main advantage of this control is the ability to decouple the flux and torque and control them independently. Controlling the d-axis current, the flux linkage with the stator can be adjusted and similarly controlling the q-axis current, torque can be controlled. To achieve MTPA, I_q is at maximum and I_d is maintained at zero.

In this case, the maximum current from the inverter is assumed to be seen at the q-axis. Hence I_q is taken to be equal to the amplitude of the AC output current $\sqrt{2}I_{o,max}$ which is also equal to the DC current drawn from the battery.

4.4.2. Field weakening control

At speeds above the rated speed, the back emf of the motor becomes large due to which the MTPA control strategy cannot be used to control the PMSM. The back emf of a PMSM is proportional to the magnetic flux ψ and the rotational speed of the motor ω [66]. When the back emf is larger than the stator voltage, the motor does not draw current and hence the power becomes zero. Thereby, the PMSM fails to provide torque to increase the speed of the motor.

The rising back emf needs to be reduced to reach higher motor speeds. To reduce the back-emf, the magnetic flux of rotor magnets is to be reduced. However, this flux is not controllable. Hence, the air-gap flux is weakened using the direct-axis current [67] and this control method is called 'Flux Weakening' control. Using this control strategy, higher motor speeds can be utilised.

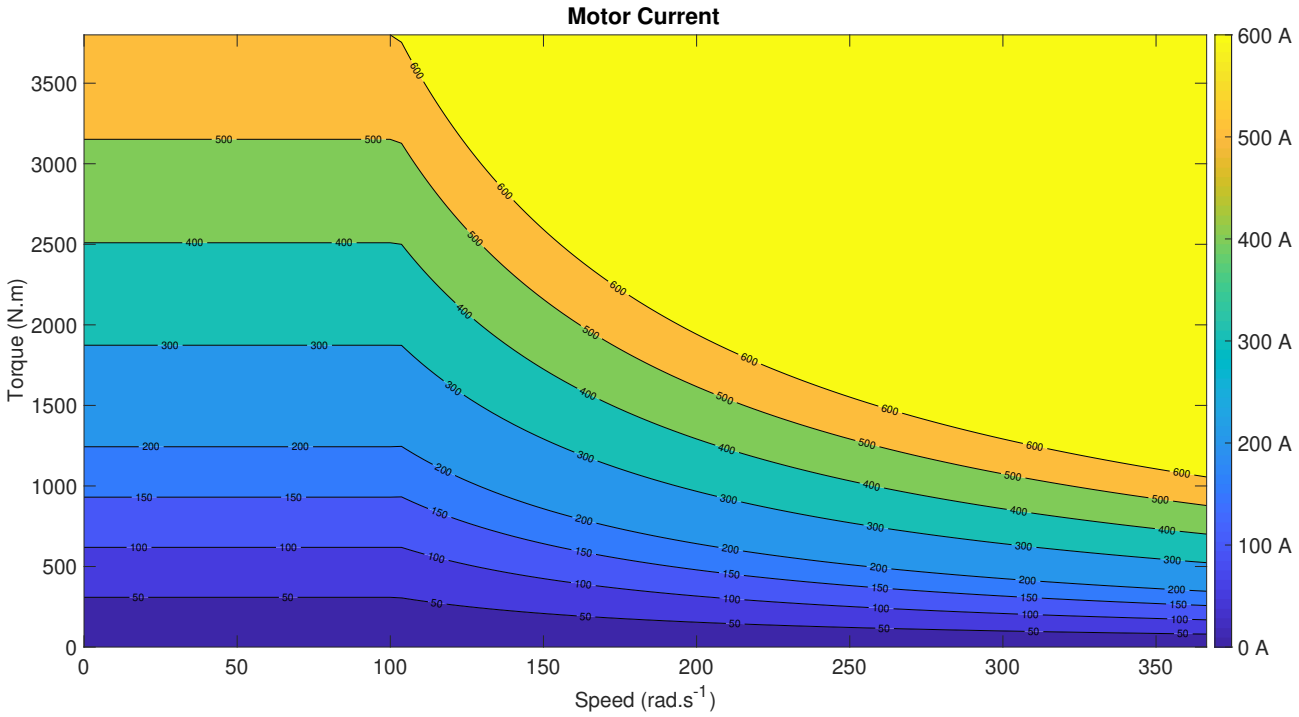

Figure 4.1: Current (in A) plotted against motor torque vs speed

In this research, sufficient information is not available to calculate the d-axis and q-axis current during flux-weakening control. Therefore, in this project, to calculate the amplitude of the current flowing through the inverter circuit during this control, the motor torque constant and back-emf constant is used.

$$\text{Torque constant, } k_T = \frac{T}{I_{amp}} \tag{4.14}$$

where, T is the motor torque and I_m is the amplitude of the three phase current. For calculating current below the rated speed, the value of k_T is taken to be 6.33 as the peak motor torque 3800 Nm and corresponding motor current is 600 A.

Below the rated speed, the torque constant remains the same. But at higher motor speeds, the current is not linearly proportional to the torque due to flux weakening control. So, in this region, the back-emf constant is used. In permanent magnet machines, the torque constant is numerically equal to the back-emf constant [68]. This constant is given by the formula,

$$\text{Back-emf constant, } k_e = \frac{V_{rated}}{\omega} \tag{4.15}$$

where, V_{rated} is the rated voltage of the motor and ω is the speed of the motor.

Using the above equation, the back-emf constant can be calculated from the voltage applied and the motor speed. Since this value is equal to the torque constant, it is used in the torque constant equation 4.14 to calculate the current amplitude as shown below.

$$I_{amp} = \frac{T}{k_e} \tag{4.16}$$

Using the above relations, the peak current drawn by the motor over the entire speed range is calculated which is in turn used to estimate the inverter losses. Figure 4.1 shows the calculated current values using the above logic. The values also match with the expected current from the motor specification sheet.

4.5. Inverter Efficiency Map

With the help of the calculated losses, the total inverter efficiency is estimated across the range of motor torque and speed to form an efficiency map. Efficiency is defined as the output power divided by the input power and in this case, the output power is the power fed to the motor and the input power is the power from the battery

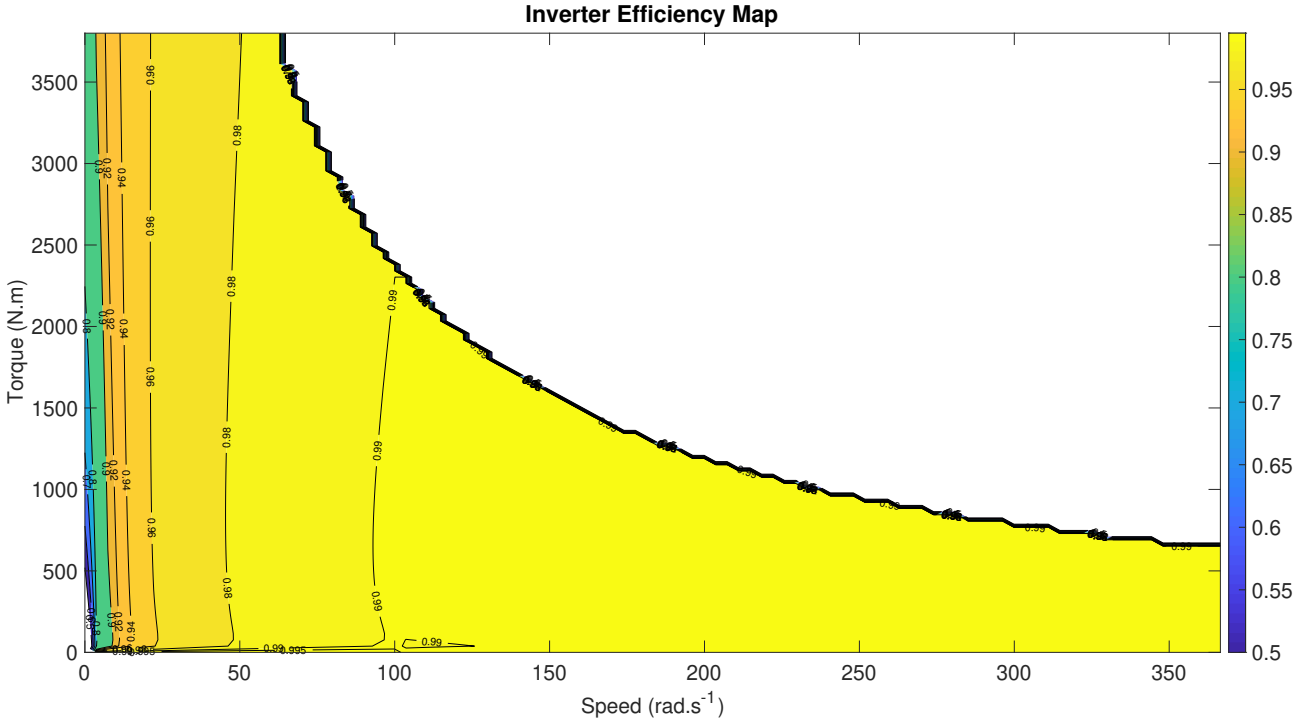

Figure 4.2: Inverter Efficiency Map plotted against the motor torque vs speed

pack. The motor input power is taken as calculated in chapter 3 and the total inverter power loss is given by the equation 4.13. These data are used to calculate the inverter efficiency using the following formula.

$$\eta_{inv} = \frac{\text{output power}}{\text{input power}} = \frac{\text{motor input power}}{\text{motor input power} + \text{inverter losses}}$$

$$\eta_{inv} = \frac{T\omega + k_c T^2 + k_h \omega + k_{ed}\omega^2 + k_w \omega^3}{(T\omega + k_c T^2 + k_h \omega + k_{ed}\omega^2 + k_w \omega^3) + P_{inv}} \tag{4.17}$$

Furthermore, the inverter efficiency changes when the vehicle is braking. This is because of regenerative braking. During regeneration, the input power to the inverter is the power generated by the motor due to generator action. The output power is the power fed to recharge the battery. Hence, the efficiency equation can be rewritten as

$$\eta_{inv,g} = \frac{\text{output power}}{\text{input power}} = \frac{\text{regenerated power} - \text{inverter losses}}{\text{regenerated power}}$$

$$\eta_{inv,g} = \frac{T\omega - \left(k_c T^2 + k_h \omega + k_{ed}\omega^2 + k_w \omega^3\right) - P_{inv}}{T\omega - (k_c T^2 + k_h \omega + k_{ed}\omega^2 + k_w \omega^3)} \tag{4.18}$$

Using the above relationship, the efficiency map is plotted for driving region is seen in the figure 4.2. Here, it can be noticed that at higher speeds the inverter has higher efficiency due to the lower currents flowing through the switches contributing to lower losses. However, at high starting currents, there is room for improvement of efficiency.

The inverter efficiency map (in figure 4.17) is combined with the motor efficiency map to obtain the overall ELFA motor drive's efficiency map which is further used in the model to estimate the power loss which will be closer to reality.

The following plots of the inverter losses are obtained by calculating individual switch losses and scaling it up to an inverter level. It can be noticed that both the losses are directly influenced by the current through the switches and this can be observed especially in the flux weakening region of the motor. The switching losses and the conduction losses of the inverter built using the selected IGBT module are shown below.

The output signal from the model is sum of the power signal obtained from the motor model and the inverter losses calculated in this chapter. Another power that is to be taken into account is the auxiliary power. Hence, this value is added to the output signal of the inverter model to obtain the power drawn from battery during driving or the power fed into the battery during regenerative braking.

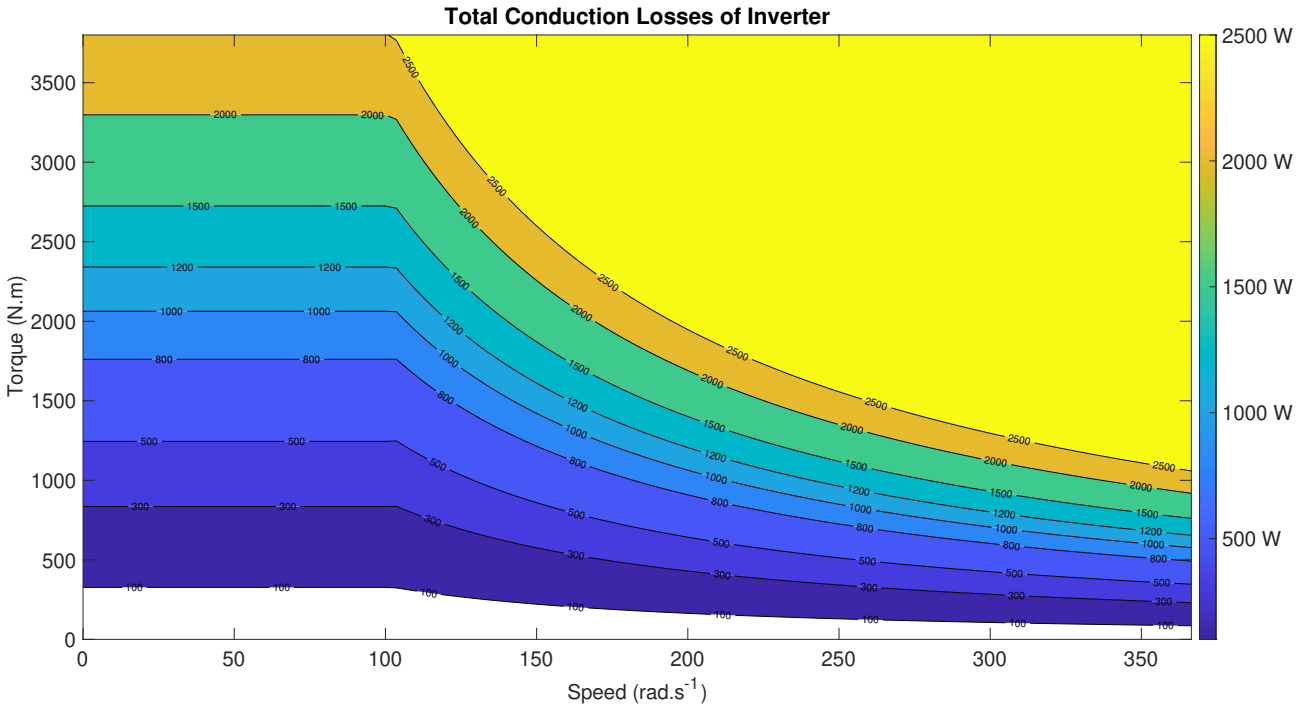

Figure 4.3: Inverter Conduction Losses (in W) plotted against motor torque vs speed

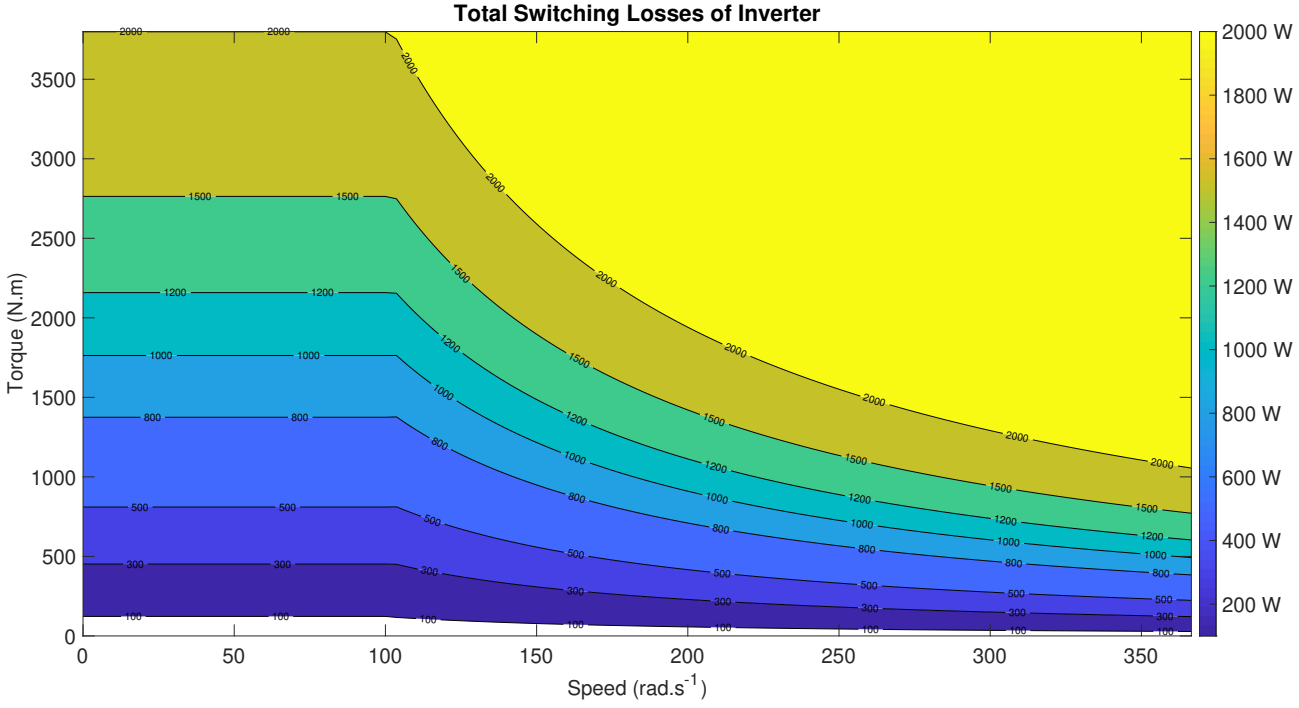

Figure 4.4: Inverter Switching Losses (in W) plotted against motor torque vs speed

5

Simulation Results and Sensitivity Analysis

In this chapter, the model is simulated repeated by varying different truck parameters based on the available data and its influence of the energy efficiency on the BEV is tabulated. This analysis is summarised at the end of the chapter to draw conclusions.

5.1. Sensitivity Analysis

Sensitivity analysis is the study of how uncertainties in the input of the model affect the output response [69]. This study helps in defining the relative importance of each input parameter to the model. To perform the sensitivity analysis, a range of parameters are identified that have a significant influence on the energy efficiency of a heavy-duty BEV [70].

Table 5.1 lists the parameters taken for the sensitivity study and the default values taken for the simulation. Some of these values of these parameters are mentioned in per unit due to confidentiality reasons. For example, for this analysis, multiple values of aerodynamic drag are used. So, one value is taken as standard and other values are converter to its per unit value as seen in table 5.2.

5.1.1. Aerodynamic Drag and Frontal Area

Aerodynamic resistance is one of the major contributors of resistive force at high velocities. It is directly proportional to the square of the truck velocity. We know that the aerodynamic resistance can be calculated using equation 2.2 as explained in chapter 3.

$$F_{aero} = \frac{\rho}{2} \times C_d \times A_f \times (v_{truck})^2$$

From this equation, it can be noticed that the product of coefficient of aerodynamic drag and frontal area directly contributes to this resistive force. This means that having an aerodynamic body for the truck can notably improve the energy consumed at higher speeds. The aerodynamic resistance and rolling resistance losses are pure energy losses, and they cannot be retrieved by regenerative braking unlike potential and kinetic (acceleration) energy [71].

For this purpose, three kinds of aerodynamic aids are used in these trucks to reduce the aerodynamic drag coefficient and improve energy efficiency. Spoilers, fenders, and sideskirts as shown in 5.1 are the different

Parameters	Value
Aerodynamic drag x Frontal Area	1 p.u.
Mass of the truck	25000 kg
Co-efficient of rolling resistance	1 p.u.
Gear efficiency	1 p.u.
Radius of the wheel	0.4748 m
Auxiliary System	12.5 kW
Minimum regenerative speed	0 km/h
Battery Pack	150 kW
Energy Density	268.4 Wh/kg

Table 5.1: List of parameters and the value taken as standard for the sensitivity analysis

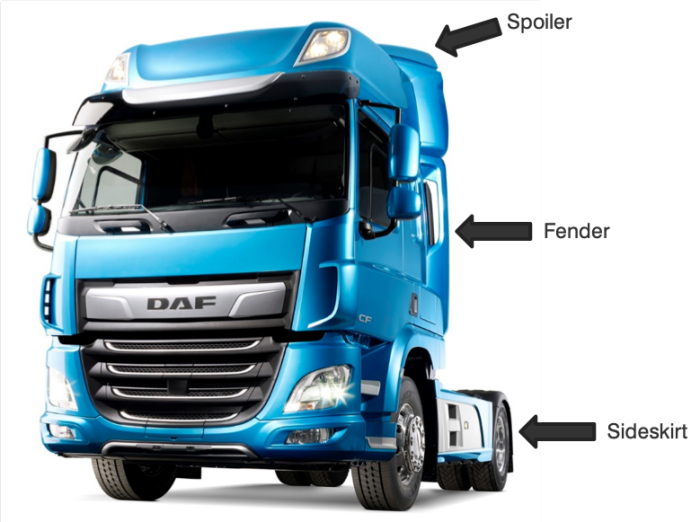

Figure 5.1: Different aids used to improve aerodynamics of the truck

	Spoiler	Fender	Sideskirt	CdxA [m2]	Energy Efficiency [kWh/km]	Range for 150kWh [km]
Aerodynamic Drag x Frontal Area	✓	✓	✓	1	1.4514	103.35
	✓	✓	×	1.04	1.4651	102.38
	✓	×	×	1.14	1.5032	99.79
	×	×	✓	1.37	1.5909	94.29
	×	×	×	1.41	1.6044	93.49

Table 5.2: Sensitivity Analysis of Drag Coefficient and Frontal Area

aerodynamic aids used. Based on the wind tunnel test data, different values of the product of drag and frontal area are taken for simulation, and this is shown in the table below in per unit (p.u.) for confidentiality reasons. The powertrain model is simulated, and the energy efficiency in terms of kWh/km for the different values are tabulated.

From table 5.2, it can be seen that the most aerodynamic truck can achieve a range which is 10.55% more than the least aerodynamic truck. A 10.55% range improvement is significant for medium-duty and heavy-duty BEVs for both urban and long-distance distribution applications. This makes the product of the drag coefficient and the frontal area key features in extending the driving range of the BEV.

5.1.2. Mass of the truck

Truck mass is a very sensitive parameter than has an immense influence on the range of the BEV. The mass of a distribution truck in a city is continuously varying due to loading and unloading at various points. However, based on the field data, an average weight that is observed in a distribution BEV is taken as a reference for the sensitivity test.

The energy efficiency of the heavy-duty BEV at full load and no-load is then taken and simulated to understand the impact the truck mass has on its range. The Gross Combination Mass (GCM) is the maximum weight that the truck can carry, which is the combined weight of the truck and the trailer with a full load. The Gross Vehicle Mass (GVM) is the total weight of the truck, including the driver, battery, and payload. Here, GCM is 37 tons, and the GVM is 9.7 tons. An intermediate weight of 25 tons is taken as the reference weight in simulations throughout the sensitivity analysis.

	Truck Mass [kg]	Energy Efficiency [kWh/km]	Range for 150kWh battery [km]
Mass of the truck (Max GCM)	37000	1.8169	82.56
Mass of the truck (Partial Load)	25000	1.4514	103.35
Mass of the truck (GVM)	9700	0.8784	170.77

Table 5.3: Sensitivity Analysis of Mass of the Vehicle

	Co-efficient of Rolling Resistance [p.u.]	Energy Efficiency [kWh/km]	Range for 150kWh Battery [km]
C_r (max)	1.36	1.6522	90.79
C_r (std)	1	1.4514	103.35
C_r (min)	0.73	1.1796	127.16

Table 5.4: Sensitivity Analysis of Coefficient of Rolling Resistance

	Gear Efficiency [% p.u.]	Energy Efficiency [kWh/km]	Range for 150kWh battery [km]
Actual	1	1.4514	103.35
+2%	1.02	1.4304	104.87
+5%	1.05	1.4006	107.10

Table 5.5: Sensitivity Analysis of Transmission Efficiency

From table 5.3, it is observed that a decrease of 12 tons from full-load can improve the range by 25.18%. For comparison, a weight of 1000 kgs was deducted from the vehicle mass of 25 tons, and the model was simulated. An improvement of 5.47% in range was observed in a change of just 1000 kgs. From this, we can see that the range is very responsive to the truck mass. Hence, the real-time energy efficiency can be expected to be better than the simulated efficiency due to constant loading and unloading of the payload.

5.1.3. Coefficient of Rolling Resistance

Coefficient of rolling resistance is a critical parameter that has a direct influence of the rolling resistance experienced by the vehicle. Various factors can affect this coefficient. Some of them are the properties of the tyres, vehicle driving speeds, weather conditions and the road surface. The road surface includes stiffness and macro-texture of the asphalt [72][20][70]. The rolling resistive force is caused by the hysteresis effects during deformation of the tyre on a hard surface [20]. Some factors that affect the deformation are the type of tyres, surface temperatures and inflating pressure.

A standard method for the measurement of the coefficient of rolling friction has not been established [70] and hence, researchers assume different values for C_r. According to the data collected by the company, a range is selected for the rolling friction coefficient for the heavy-duty BEV. This range is applied in our study in per unit (p.u.) in the table below, and simulation is run to observe the change in range achieved.

From the table 5.4, it is seen that when the coefficient of rolling resistance is at its maximum value, the range of the BEV decreases by 12.15%. However, when the coefficient of rolling resistance is at its minimum value, the range of the BEV increases by 23.04%. This considerable variation in the range for small variations in the coefficient of rolling resistance makes it a highly sensitive parameter.

5.1.4. Transmission Efficiency

The mechanical power losses experienced by the powertrain also influences the range of BEVs. It is for the same reason that most electric vehicle manufacturers prefer to use a fixed reduction gear and differential. This design has reduced transmission losses since only one gear and differential is involved, and it also requires almost negligible maintenance.

The efficiency of transmission systems is generally considered to be a fixed value; however, it varies as the torque and speed vary [73]. To predict the loss and to calculate the efficiency of the drivetrain at different running conditions, it is necessary to build a dynamic model.

The drivetrain losses can be classified into two types: torque dependent losses and torque independent losses. The torque dependent losses arise from the rolling and sliding movements of the mechanical parts such as gears and bearing. Torque independent losses are also known as speed or spin losses, and they arise from the lubrication method. Some examples of such losses are windage and oil churning losses. These losses are seen due to the air and oil surrounding the gears [73]. Modelling all these losses would require a fluid-mechanics based model which is a considerably more difficult task. Hence, a significant amount of research is based on dimensional analysis or experimental data.

In this model, the data provided by the company is directly used; hence losses are not individually calculated for improvement recommendation. In this sensitivity study, the primary focus is on investigating how much range improvement can be achieved by improving the efficiency of the transmission system.

In table 5.5, two cases along with the actual value of transmission efficiency is chosen in p.u. It can be seen that a 2% improvement in the driveline efficiency can increase the range up to 1.5%. For improvement of 5%

Auxiliary System [kW]	Energy Efficiency [kWh/km]	Range for 150kWh Battery [km]
5	1.1527	130.13
12.5	1.4514	103.35
20	1.7501	85.71

Table 5.6: Sensitivity Analysis of Auxiliary System

Minimum Regenerative Speed [km/hr]	Energy Efficiency [kWh/km]	Range for 150kWh battery [km]
0	1.4514	103.35
5	1.454	103.16
10	1.4622	102.59
15	1.4761	101.62

Table 5.7: Analysis of Minimum Regenerative Speed

in the transmission efficiency and improved range of up to 3.6% can be obtained. Hence, it is recommended to explore options to improve transmission efficiency in future work.

5.1.5. Auxiliary System

The auxiliary system is a core part of all vehicles, and the power drawn by this system has a dramatic impact on the range of the BEV. Energy consumed by the auxiliaries varies depending on the external conditions such as illumination, temperature, etc. and driver behaviour [70]. Some of the units in the auxiliary system are AC compressors, coolant pump, power steering, power brakes, and other miscellaneous factors like lights, infotainment system, power-assisted seats, windows, locks, etc.

In [74], the auxiliary system used by Scania is studied to model and control the auxiliary loads. From this study, based on the minimum and maximum of the power consumed by auxiliaries, a range of 5kW to 30 kW (of power consumption) is seen. Further research seen in [75], verifies methods for reducing the energy utilisation by optimised control of the auxiliary system and selection of energy-efficient components with a Scania hybrid fuel cell concept bus. In this study, the power consumed by auxiliary is limited to 20 kW over the driving range. Hence, for this sensitivity analysis, the energy efficiency of the powertrain is examined over a range of 5kW to 20kW of power consumed by auxiliary subsystem.

From table 5.6, it is seen that using minimum power of 5KW for auxiliary can give a range improvement of 25.92%. However, when up to 20kW power is continuously utilised by the auxiliary system, the range is seen to decrease by 17.06%.

5.2. Regenerative Braking

As we know, regenerative braking plays an essential role in improving the range of BEVs by recuperating the kinetic and potential energy that is lost during braking. Heavy-duty BEVs have very high potential energy that can be recovered during braking which makes optimisation of regeneration more critical. In this section, the regenerative model and the parameters associated are analysed to reflect their effects on the electric vehicle's range.

5.2.1. Minimum regenerative speed

The minimum speed for regeneration is chosen as a factor that is considered for observing the range of the BEV because of the effect it has on cell ageing. From figure 3.5 in chapter 3, it is observed that the operating points of the motor are clustered at low speeds. This causes very short charging and discharging cycles of the battery pack at high currents which leads to 'micro-cycling' that affects the lifetime of the battery pack [56]. Also, at low motor rotational speeds, electrical machines generate low electromotive force thereby charging the battery pack at low voltages [20].

For the above reasons, a minimum speed limit is to be defined by analysing its effect on the ageing of Li-ion cells. For understanding the influence of the value of minimum regenerative speed on energy efficiency, the model is simulated for different speed limits. The range of this parameter is taken between 0 and 15 km/h following the study in [70].

From the table 5.7, it can be observed that the minimum regenerative speed limit have minimal effect on the energy efficiency of the BEV. Setting a 5 km/h limit only decreases the range by 0.15%, which is negligibly

Braking Strategy	Energy Efficiency [kWh/km]	Distance for 150kWh battery [km]
Parallel Regenerative Braking	1.66	90
Serial Regenerative Braking	1.45	103

Table 5.8: Sensitivity analysis of different regenerative braking strategies

small. However, a higher speed limit of 15 km/h decreases the range by 1.64%, which is a considerable amount of potential energy lost. Hence, optimisation of this value to improve the lifetime of the battery can be done without the concern of having an impact on the range.

5.2.2. Maximum SoC for regenerative braking

The maximum limit of SOC for regenerative braking is an important parameter that is to be considered in the regenerative braking strategy. The reason why the recuperation of energy is limited during braking at high SOC of the battery pack is to prevent overcharging due to high voltages.

Charging of the cell above the cut-off voltage prescribed by the manufacturer is defined as overcharging. Overcharging increases the capacity by a small amount but the cycle life is affected at later stages [76]. Various other effects due to overcharging of the cell mentioned in [76] are temperature rise, increase in internal resistance, decomposition of binder, etc. Excessive heating of the battery also increases the heat rejection requirement of the cooling system.

As the battery model is not included in the model, the effect of limiting regenerative braking is not studied. However, it is highly recommended to study this parameter during the testing of the battery pack.

5.2.3. Difference between Serial and Parallel Regenerative Braking

In the simulation results in this chapter, the serial regenerative braking strategy is implemented. To understand the difference between the two regenerative braking strategies discussed in chapter 3, both the strategies are implemented, and the energy efficiencies that were achieved are tabulated.

From the table 5.8, it can be observed that up to 14.53% improvement in the range is achieved just by using the appropriate braking strategy.

5.3. Radius of the wheel

The radius of the wheel is an important aspect of a powertrain design. The wheel size influences selection of motor, transmission gears, rolling resistance, etc. In this section, the focus will be on the impact of change in wheel size on the range as per the current design on the powertrain. There are a few differences that can be observed in the performance of the vehicle based on the size of the wheel.

In terms of handling, smaller wheels have an advantage over the bigger wheel as each rotation covers a shorter distance. In most vehicles, bigger wheels mean better grip and stability due to the wider contact path leading to improved performance, especially during cornering [77]. Additionally, a bigger wheel in the powertrain also increases the speed range of the vehicle. An increase in speed range is seen because the maximum speed that the motor operates when the wheel size is increased reduces, which opens up more speed range of the motor that can be utilised. The simulation results, seen below in figure 5.2, showcase the operating points of the powertrain with changes only in the wheel radius. These results are discussed further below.

An obvious disadvantage in installing bigger wheels is that it will increase the overall weight of the vehicle. As the increase is weight to the overall weight of the truck is negligibly small, this change is not incorporated in the simulation results. However, it is to be noted that a larger wheel will have more inertia than a smaller wheel and hence, more torque is required to achieve the same level of acceleration. During deceleration, this will account for a reduction in the braking distance, which is advantageous for heavy-duty vehicles. Another factor acting to the disadvantage of bigger wheels is that these wheels tend to have higher rolling resistance [78][77]. As seen earlier, the coefficient of rolling resistance has a significant effect on the range and energy efficiency.

To observe the effect of the wheel size on the energy efficiency, few wheels currently used in the truck model taken are used. Table 5.9 shows the energy efficiencies achieved for different wheel sizes. It is seen that the more range can be achieved with bigger wheel radii. As we know, the bigger wheel has more inertia, and the torque required for acceleration is higher compared to a smaller wheel. So, the losses are expected to be higher as higher current is needed by the truck with a bigger wheel for high torques. To understand the operation, the motor operating points are obtained by simulating the model for two-wheel radii and plotted against the motor

	Radius of the wheel [m]	Energy Efficiency [kWh/km]	Distance for 100kWh battery [km]
295/60R22.5	0.4627	1.4567	102.97
295/80R22.5	0.5217	1.3315	112.65
315/60R22.5	0.4748	1.4514	103.35
315/70R22.5	0.5062	1.3643	109.95
315/80R22.5	0.5377	1.3259	113.13

Table 5.9: Sensitivity analysis of different wheel radii

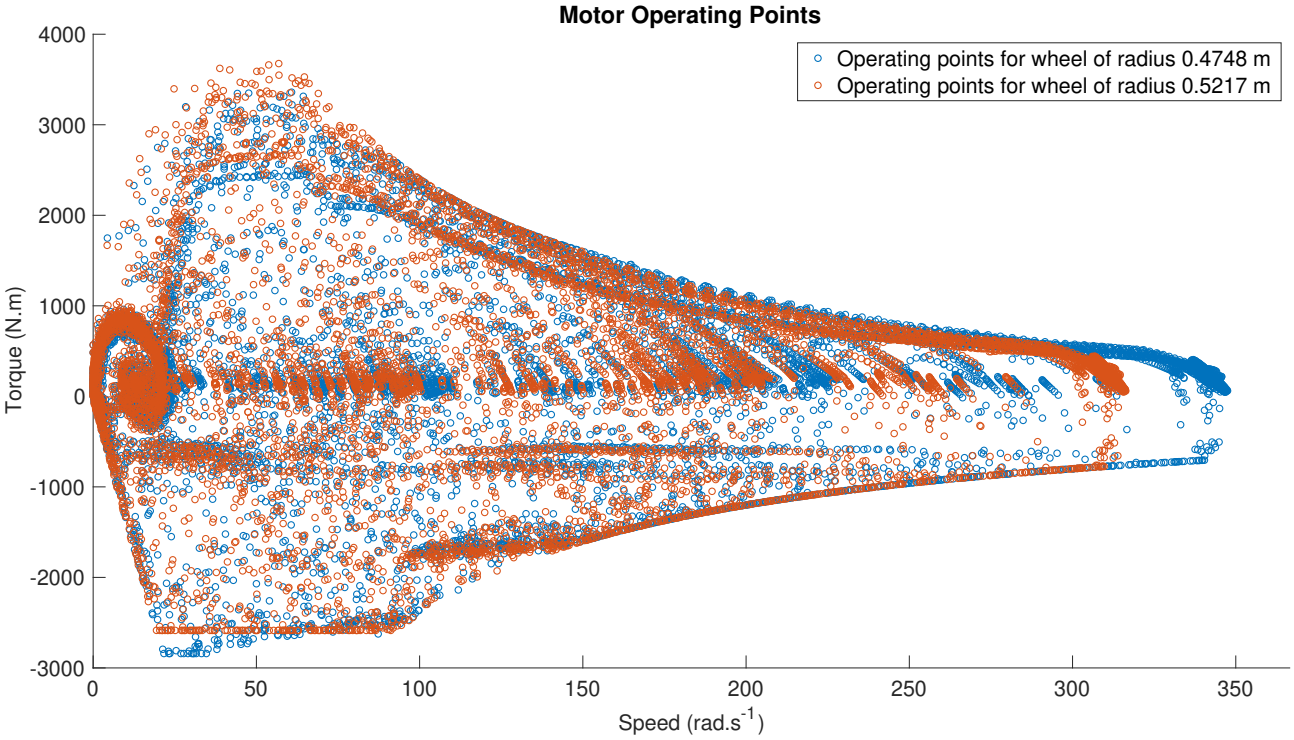

Figure 5.2: Operating points of the motor in one drive cycle with two different wheel radius

torque and motor speed, as seen in figure 5.2. The bigger wheel represents the wheel 295/80R22.5 of radius 0.5217 m, and a smaller wheel represent the wheel 315/60R22.5 of radius 0.4748 m.

From the figure 5.2, it can be seen that the operating points of the motor in the powertrain with bigger wheel are at lower speed and higher torques compared to that of the powertrain with smaller wheel size. This signifies that there is a considerable difference in the losses in motor drive. All the motor and inverter losses are obtained for both wheel sizes, and a bar chart is plotted in the figure 5.4 for easy understanding. It can be seen that the major difference is in the losses contributed by the motor.

From figure 5.3, the following conclusions can be derived. The loss components that are directly dependant on the speed of the motor such as hysteresis, eddy-current, and windage loss are reduced when a bigger wheel is used. As expected, the copper losses increase for the bigger wheel as higher torque/current is drawn from the motor. It is to be noted that the copper losses caused by high currents contribute to high temperatures in the electrical machine thereby putting stress on the cooling system.

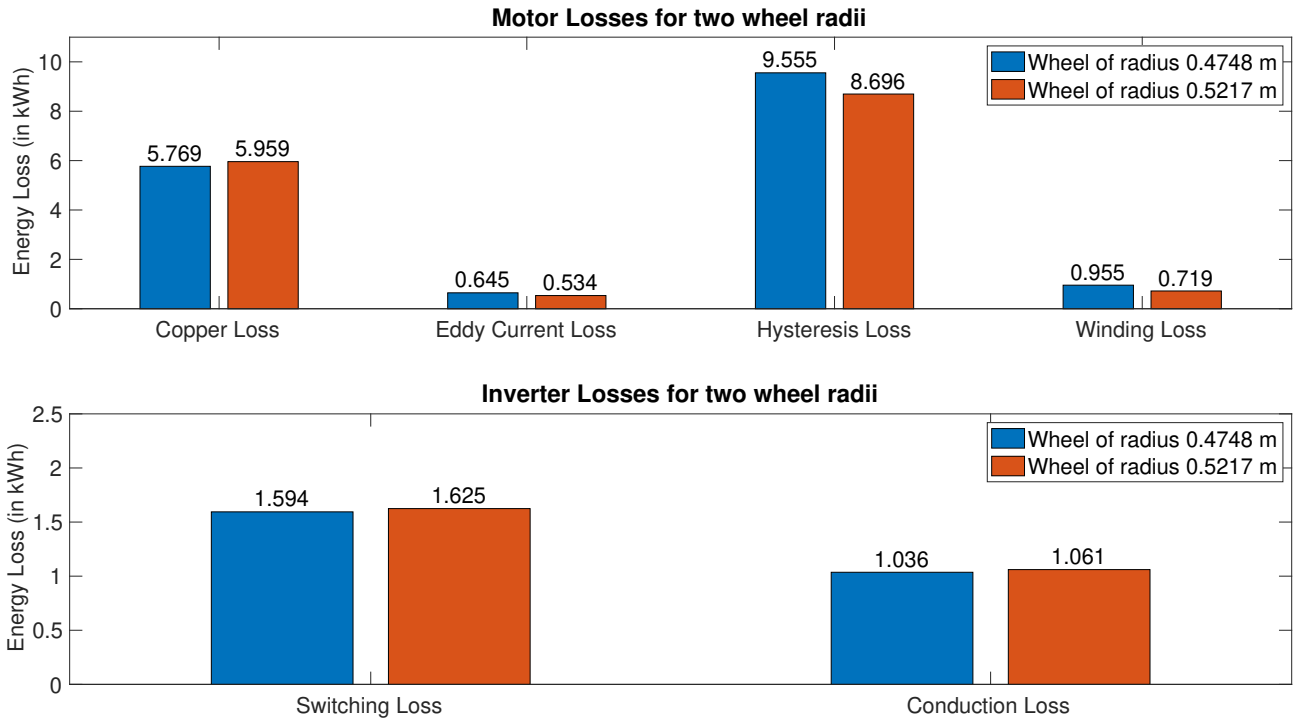

Figure 5.3: Comparison of the energy lost due to the individual motor and inverter losses with two different radii for the wheel

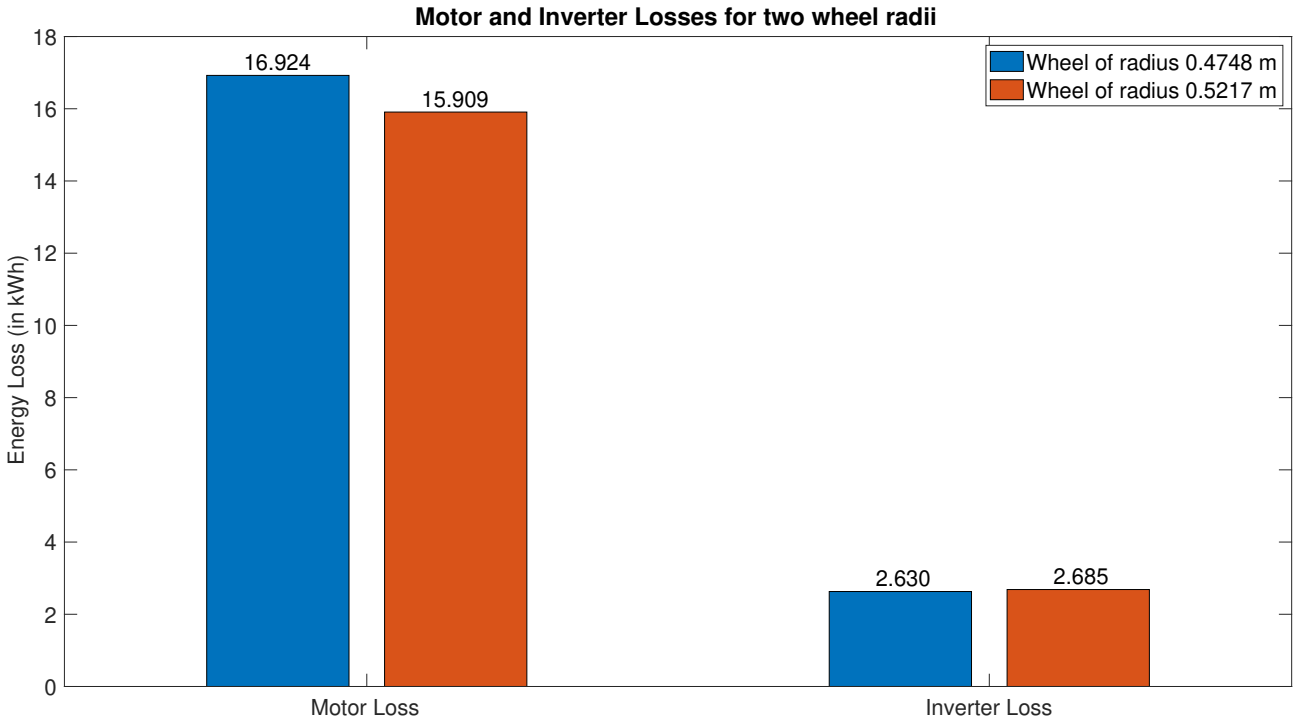

Figure 5.4: Comparison of the net energy lost at the motor and inverter for model with two different radii for the wheel

Figure 5.5: Reading Tyre Sizes [79]

5.4. Summary

In this chapter, various parameters are analysed individually and its effect on the range is studied. However, it is hard to obtain an overall perspective to identify the most sensitive elements and to prioritise the elements for design improvements. Hence, a Pareto chart is used to represent the percentage improvement in descending order with a bar chart and its cumulative value with a line graph.

Table 5.10 shows the list of most sensitive parameters with the reference value that was used throughout the study and the percentage increase in the BEV range for a 5% change of this value. For the radius of the wheel and transmission efficiency, 5% is increased from the reference value while for other parameters 5% is decreased. For each change, the simulation is run and the new range is calculated. Comparing with the previously obtained range value, the percentage improvement is calculated and tabulated.

Sensitive Parameters		**% increase in range for a 5% change**
Truck mass	25000 kg	7.98
Rolling Resistance Coefficient	1 p.u.	7.32
Radius of the wheel	0.4748 m	6.13
Transmission Efficiency	1 p.u.	3.64
Auxiliary System	12.5 kW	1.73
Aerodynamic drag	1 p.u.	1.30

Table 5.10: Summary of percentage increase in the range based on 5 percentage change in the parameter value

Using values from table 5.10, the Pareto chart is visualised in figure 5.6. The blue coloured bar chart is arranged in descending order based on the percentage value of the improvement in range while the red line signifies the cumulative percentage of the range improvements. From this figure, we understand that the truck mass and coefficient of rolling resistance are the most influencing parameters.

Based on design choices, a wheel with a larger radius and the energy-efficient auxiliary system will improve the range. However, while using larger wheels, the impact it has on the thermal management system will be interesting to study in the future. As improving the transmission efficiency is more expensive than the other options, this is given lower priority. Finally, opting for the most aerodynamic body for the truck and energy-efficient design of auxiliaries are promising ways to improve the energy efficiency of a BEV.

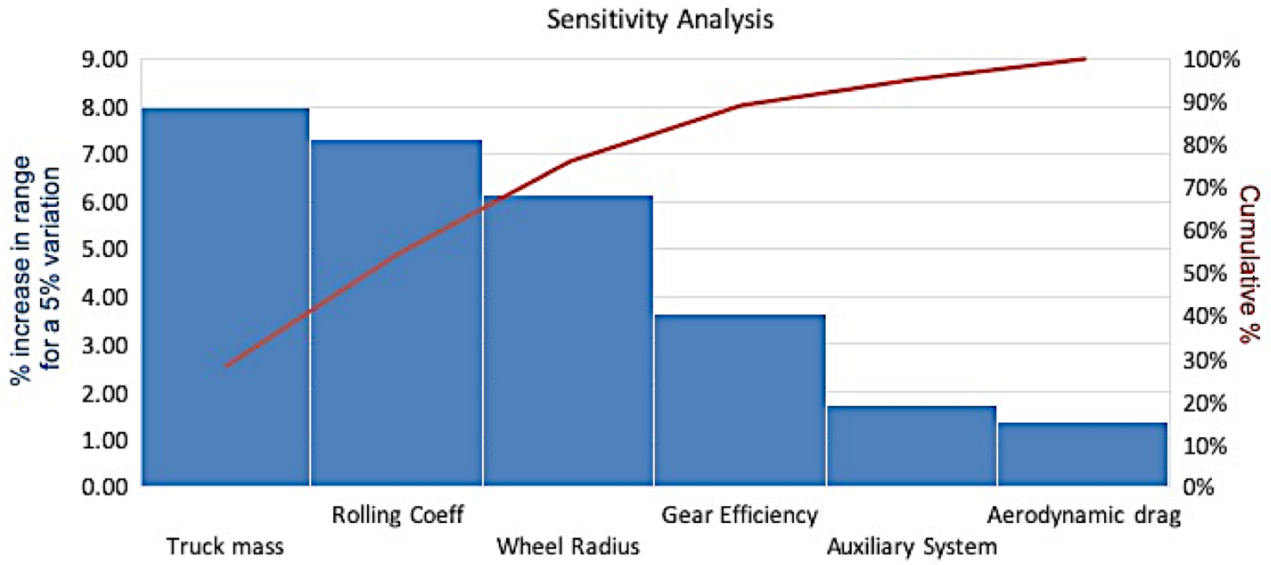

Figure 5.6: Pareto chart displaying impact of different sensitivities

6

Comparison of Powertrain Architectures

Powertrain architecture is an important factor in an electric vehicle. It is necessary to understand the topology of the powertrain and the power flow among the components. The design of the powertrain architecture and component selection plays a significant role in determining energy efficiency, future design, control strategy, and optimisations [19].

In this chapter, two kinds of powertrain architectures are studied in detail and modelled to analyse the improvement in the energy efficiency of the BEV. Firstly, two-speed transmission with a single motor powertrain is modelled with the same 200kW motor as used in the single motor fixed reduction powertrain. In the second part of the chapter, a dual-motor powertrain is explored with two 160kW motors instead of 200kW motor. The approach taken to realise this powertrain architecture is also further detailed.

6.1. Single motor powertrain with two-speed transmission

In this powertrain architecture, a single motor with a two-speed transmission is used to drive the truck. The motor used is the same 200kW permanent magnet synchronous motor from the single motor powertrain used in the sensitivity analysis. All of the components in the powertrain is retained except the transmission. In this case, two gears of different gear ratios are used and as the model is not following an existing transmission, the gear ratios are arbitrarily chosen by trial and error with the focus to improve the energy efficiency. The gear ratios can be optimised to obtain maximum improvement in energy efficiency.

6.1.1. Transmission

As transmission is the only component that is being substituted from the existing powertrain architecture, the changes and the assumptions are listed in this subsection. The first gear taken is the same reduction gear of 7.21 gear ratio and the second gear is assumed to be a reduction gear of lower gear ratio of 5.5. It is to be noted that this value is not based on an existing transmission. Hence, future research in optimising the gear ratios for the first and second gear is recommended.

Another important factor which is assumed in this simulation is the gear shift map. This is nothing but the speed at which the gear is shifted from first gear to the second. However, this shift is not a straightforward speed value. It is based on the amount of acceleration required from the driver pedal input and the current speed of the vehicle. This is further explained in detail in [41]. In the following simulation, the gear shift map is simplified and a speed of 35 km/h is assumed to be the speed at which the gear shifts from first gear to the second and vice versa. This transition between the two gears is to be studied in detail and optimised to obtain maximum efficiency and improved handling of the BEV.

The last assumption taken in implementing this powertrain is the transmission efficiency. As discussed in 2.5.3, the efficiency of 2-speed transmission can be comparatively lower [38]. However, for this model, the transmission efficiency is assumed to be the same as the efficiency of a fixed-gear transmission. This factor is also critical in the overall driveline efficiency and the selection of this architecture because a decrease of as much as 5% of this value can reduce the range by 3.64% as seen in chapter 5.

6.1.2. Comparison with single-speed drivetrain

To understand if using a two-speed transmission is beneficial in improving the energy efficiency to a single-speed transmission, the two powertrain architectures are compared. All the standard parameters that were used in chapter 5 are retained and energy efficiency of 1.45 kWh/km is observed in the single-speed powertrain.

Parameter	Value
Gear Ratio 1	7.21
Gear Ratio 2	5.5
Gearshift speed	35 km/h

Table 6.1: Values assumed in the single motor 2-speed powertrain simulation

	Energy Efficiency [kWh/km]	Range for 150kWh [km]
Single speed transmission	1.4514	103.35
2-speed transmission	1.4265	105.15

Table 6.2: Energy efficiency comparison between powertrain with a single-speed transmission and two-speed transmission

From the simulation results of the two-speed powertrain, energy efficiency and range is tabulated and compared as seen in table 6.2.

It can be seen that by using a two-speed transmission with a second gear of lower gear ratio, the energy efficiency can be improved by 1.75%. This improvement in energy efficiency can be understood clearly by observing the operating points of the motor on the efficiency map. In figure 6.1, it can be seen that more points of operation are clustered at the higher efficiency region and lower speed thereby reducing the overall losses.

This shows that optimising the gear shift map and gear ratio values for the first and second gear could further improve the overall efficiency of the powertrain significantly. As this improvement can be achieved with minimal changes in the existing powertrain architecture, it is recommended for future works.

6.2. Dual Motor Drive System

The powertrain architecture used here is a dual-motor powertrain with all-wheel drive capabilities such that a motor is attached in the front and rear axle. This type of powertrain has two electric motors with a fixed reduction gear to each axle. The motor used in the study is high power and high torque motor and installing two such motors is not necessary. Truck manufacturers and drivers do not look for high acceleration, unlike cars. Hence, other motors that could be used as a substitute for simulation were explored.

In order to improve the energy efficiency, two strategies that can be explored for further work are using different gear ratios for the front and rear axles and turning off one of the motors to reduce losses when adequate torque can be provided by a single motor [19][27]. These strategies are not implemented or explored in this thesis work. Implementing an optimised control can improve the energy efficiency and handling performance of the vehicle. This architecture can be specifically beneficial in off-road applications such as construction sites, etc.

6.2.1. Motor and Efficiency Map

To explore the dual motor powertrain, a PMSM motor part of the same Siemens ELFA series was identified with a lower power and torque rating. Table 6.3 gives the specification of the 160 kW PMSM that is more suitable for this powertrain topology.

One of the key factors to be noted is the increase in weight of the overall powertrain due to the presence of an extra motor and inverter. Observing the specifications from table 6.3 and table 3.1, it can be assumed that using two of the motor and inverter could increase the weight of the overall electrical system by approximately 1.5 times. It is to be noted that this assumption is based on the available specification and is not tested with

Permanent Magnet Synchronous Motor	
Rated Voltage	650 V
Rated Current	210 A
Rated Power	160 kW @ 1500 rpm
Rated Torque	1500 Nm @ 210A
Max. Torque	2500 Nm @ 350A
Max. Speed	3500 rpm
Weight	<350 kg
Cooling	Water-Glycol

Table 6.3: Siemens 160kW PM Synchronous Motor Specifications

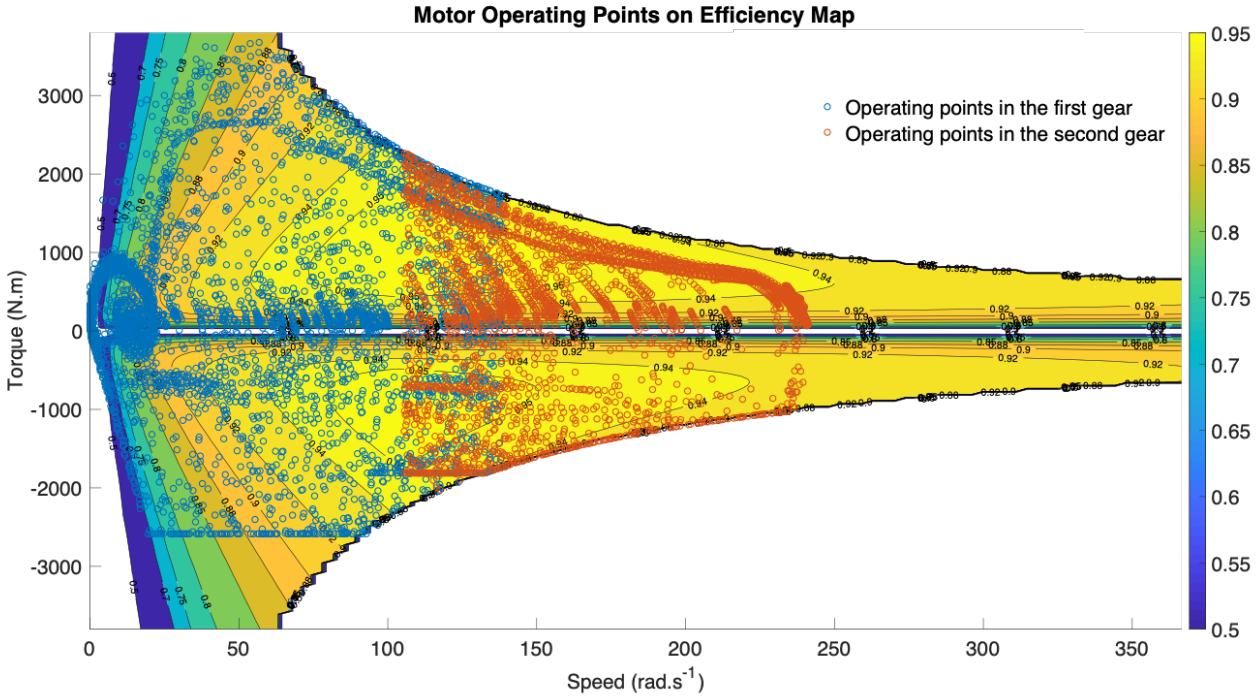

Figure 6.1: Operating points of 200kW motor in a two-speed transmission powertrain

the actual motor drive. To incorporate the increase in weight, an approximated value of 250 kg was included in the total truck mass during simulations.

Another challenge in incorporating the 160kW motor was the unavailability of an efficiency map from the manufacturer. Hence, in this study, the efficiency map of 200kW motor is fitted into the torque-speed graph of the 160kW motor by changing the y-axis scale from 0-3800 Nm of 200kW motor to 0-2500 Nm to match the torque limits of 160kW motor. This efficiency map was used as a reference efficiency map in the PSO algorithm to extract the motor loss constants. The 160kW motor is assumed to have a similar efficiency map as it is part of the same ELFA series from Siemens specifically designed for electric buses and truck applications. However, it is to be noted that this efficiency map is based on assumption and could be incorrect in the actual motor. The value of the loss constants obtained from the PSO algorithm are as listed below:

$$k_c = 0.003038$$
$$k_h = 8.1307$$
$$k_{ed} = 0.005902$$
$$k_w = 1.2079 \times 10^{-5}$$

As a motor with different specifications seen in table 6.3 is used, the inverter used also changes. Hence, for inverter module selection, the same approach, as discussed in chapter 4 is followed here as well. The inverter module that was selected for this motor was SEMIKRON SKiM304GD12T4D. Using the values from its datasheet, the inverter losses were calculated. Finally, the overall efficiency map was plotted with the motor and inverter losses. Figure 6.2 shows the efficiency map that was obtained.

6.2.2. Regenerative Braking

One of the important criteria to take into consideration is the regenerative braking strategy. From the sensitivity study conducted on the regenerative braking strategy in chapter 5, it is known that this parameter has a significant influence on the range. Hence, the serial regenerative braking strategy is applied to this architecture as well to achieve the maximum range from the BEV.

In this powertrain layout, both the front and rear axle is connected to a 160kW PMSM. In this control strategy implemented, the braking force required after the brake pedals are applied is provided equally by both the motors in the front and rear axle. When the required braking force is greater than the regenerative braking from the motors, then the remainder brake force is equally provided by the front and rear friction brakes. This control is depicted in a flowchart in figure 6.3.

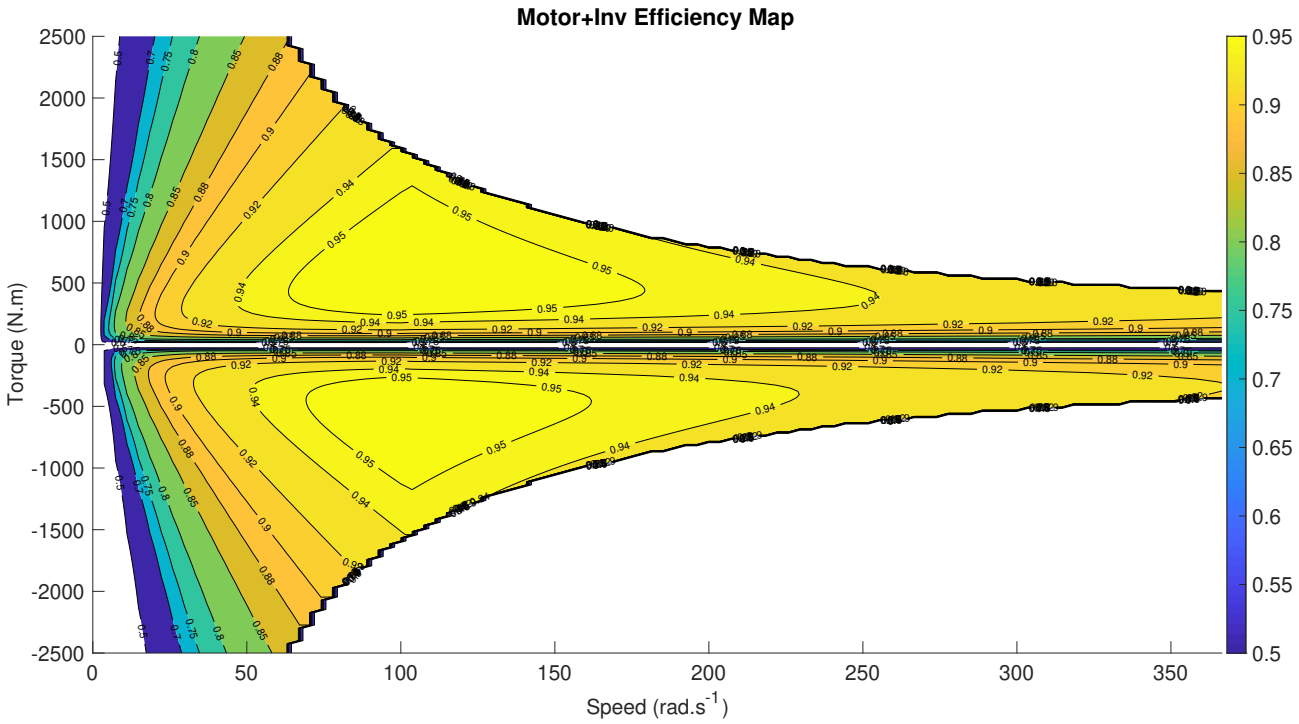

Figure 6.2: Efficiency Map of 160kW motor

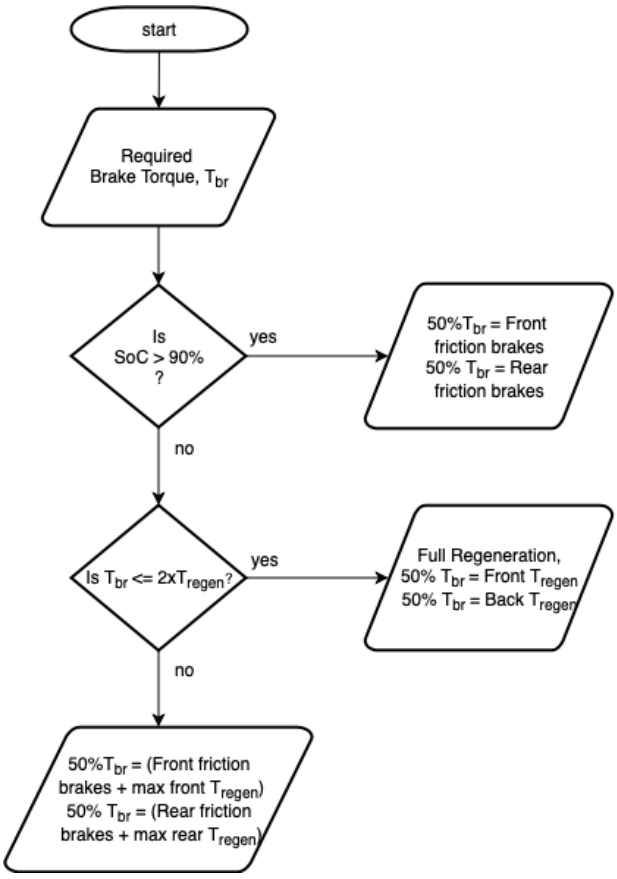

Figure 6.3: Regenerative braking control strategy flowchart for dual motor powertrain

	Energy Efficiency [kWh/km]	Range for 150kWh [km]
200kW Single motor powertrain	1.4514	103.35
160kW Dual motor powertrain	1.3301	112.77

Table 6.4: Energy efficiency comparison between single motor and dual motor powertrains

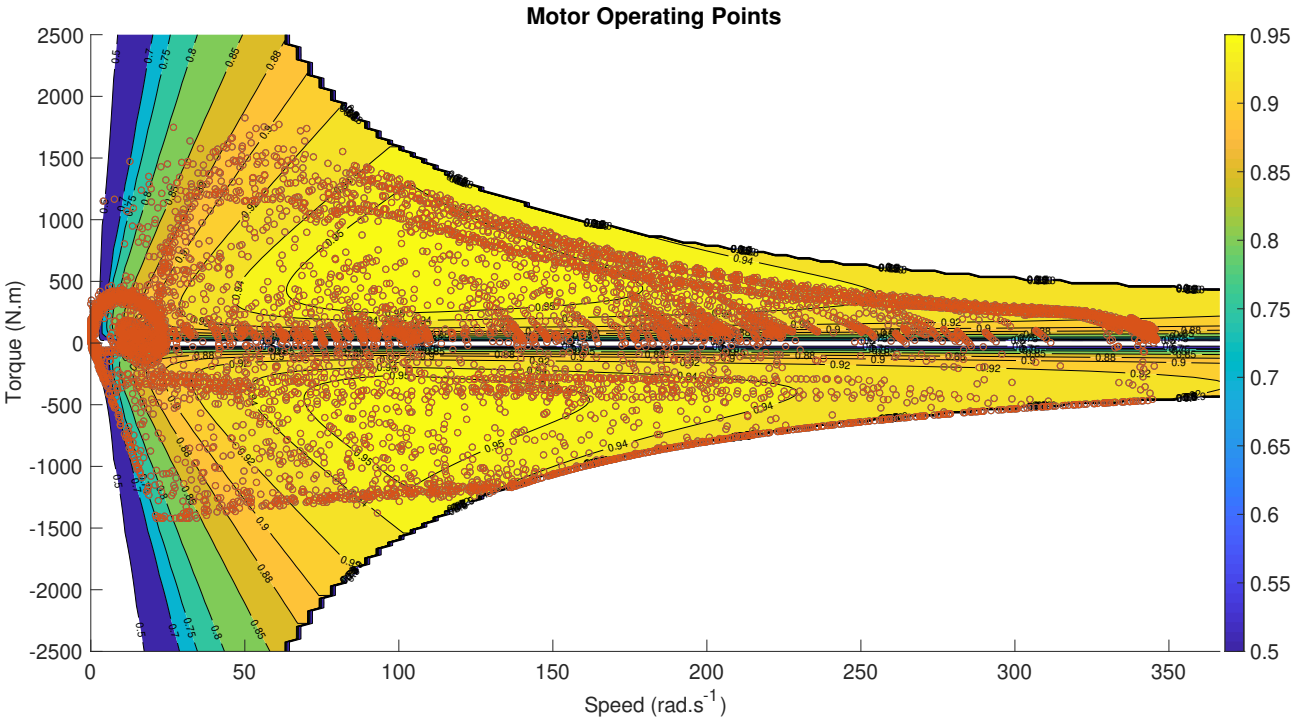

Figure 6.4: Operating points of a single 160 kW motor on its efficiency map

6.2.3. Efficiency Comparison

The dual motor powertrain model with two 160kW motor is simulated with the updated motor and inverter specifications. The energy efficiency obtained is tabulated and compared with the 200kW single motor powertrain. It can be seen that 9.11% improvement is seen in a dual-motor powertrain when compared to the 200kW single motor powertrain.

Figure 6.4 shows the operating points of one of the 160kW motors over the entire driving cycle. It can be observed that both the 160kW motors operate at low torque regions at low currents and correspondingly, the losses are also very low. This helps in achieving higher energy efficiency compared to the single-motor powertrain. Further research in this dual motor powertrain could be specifically useful for construction and off-road trucks as AWD improves handling and the overall efficiency.

The optimisation challenges mentioned in both the above-mentioned powertrains can be addressed using quasi-static or backward-facing models and the particle swarm optimisation algorithm. Such models are widely used in powertrain component size optimisation problems [10] [80] [81]. One of the challenges in using forward-facing models in such problems is the need to tune the PI controller for changes in the system.

7

Conclusions and Recommendations

The main objective of the thesis was accomplished by addressing the three research questions that were broken down from the research goal as seen in chapter 1. The electric powertrain of the heavy-duty BEV was modelled using MATLAB and Simulink. The powertrain components such as the electric motor and inverter were included in detail to understand the individual losses in the motor drive in chapters 3 and 4.

One of the limitations experienced during modelling was inadequate information on motor and inverter specifications. Hence, based on the motor ratings, an appropriate IGBT module was chosen to model the actual inverter. Owing to the limited information of the motor, the motor behaviour in the flux weakening region was approximated to realise the best possible match to the real-world operation using motor torque constant and back-emf constant. After understanding the motor and inverter operation, the corresponding components' individual losses were extracted from the existing efficiency map of the motor drive.

After calculating and understanding the losses of each powertrain component, the energy provided by the battery during a driving cycle to drive the vehicle was analysed and the energy efficiency in terms of kWh/km was obtained. Using the energy efficiency and size of the battery pack, the range of the heavy-duty BEV was estimated.

The complete powertrain model of the truck was used to perform sensitivity analysis to analyse and understand the parameters that have the most influence on the range of a BEV. From the results obtained, the most sensitive elements were identified and suggestions were made accordingly as listed below to improve the energy efficiency of the truck.

In chapter 6, different powertrain architectures were studied and modelled to understand their energy efficiencies and challenges involved.

7.1. Conclusion

Based on the detailed study and the results obtained, the following conclusions are made to answer the research questions.

- The motor loss constant namely copper loss, eddy current loss, hysteresis loss, and windage loss can be extracted from the reference efficiency map by creating an efficiency map and matching it with the reference map using particle swarm optimisation algorithm. The inverter losses namely conduction and switching losses are also calculated using simplified equations, as seen in [62] and incorporated in the overall efficiency map calculation to obtain the efficiencies over the entire torque and speed range of the machine.

- Based on the results from sensitivity analysis the following parameters are found to influence the vehicle's range the most even with small variations

  - Mass of the truck
  - Coefficient of rolling resistance
  - Radius of the wheel
  - Auxiliary System
  - Aerodynamic drag and frontal area

Hence, opting for an aerodynamic body for the truck with wheels having a larger radius and reduced rolling resistance coefficient can maximise the range of the vehicle. Improving the auxiliary system design such that the components chosen are energy efficient also increases the vehicle's range significantly. The transmission efficiency is given lower priority in future improvements due to the investment involved compared to other parameters.

To understand the reliability of this conclusion, it is important to highlight the uncertainties in this model due to inadequate information and assumptions. Some of the uncertainties are listed below

- The mass of the truck is one of the most varying values and is highly dependent on the application and payload of the truck. The truck mass was a constant value in the simulations.
- The coefficient of rolling resistance, which is one of the most sensitive elements, is also a varying element depending on the road conditions and driving behaviour. In the simulations, a constant average value was taken.
- The power drawn from the auxiliary system is not constant throughout the operation of the truck and depends on factors such as climate conditions and surrounding illumination. In this case, a constant value was chosen throughout the simulations.
- The motor losses calculated in this thesis is not accurate in the entire range of operation as the motor information that was available was inadequate. This approach makes the most out of the available motor data and the efficiency map.
- The inverter losses are simplified in this work as there is insufficient information of the inverter. The switches selected in this project were chosen based on compatibility and may not be the actual switches used in the system.

- From the different powertrain options available, two powertrain architectures are shortlisted namely single motor powertrain with a 2-speed transmission and dual-motor powertrain with the all-wheel-drive capability. These two options showed advantages over the other options in terms of simplicity in design and implementation for a production vehicle in 2020. Based on the analysis of these powertrains and simulation results, the following conclusions are drawn.
  - For a simple design with a single motor, powertrain with the 2-speed transmission can improve the energy efficiency significantly when the gear ratios and gear switching speeds are optimised accordingly. This architecture has the least changes in terms of overall design compared to the current single motor architecture. The only change, in this case, is the transmission gearbox.
  - A dual motor architecture with all-wheel drive capabilities provides improved vehicle performance which is particularly useful for the trucks used in off-road applications such as construction sites, etc. This architecture is also seen to improve the energy efficiency of the powertrain as two motors of lower power ratings correspond to lesser current and lesser heat losses. This reduces the load on the thermal management system. This powertrain also has optimisation challenges that can improve energy efficiency further. Tuning the motor control such a way that both the motors do not operate at times when it is not required and optimising the gear ratios of the front and rear axles can improve range. In this result, it is to be noted that the efficiency map of the 160kW motor used in this architecture is not obtained from the original equipment manufacturer and hence actual range may vary from the obtained range.

7.2. Future work and recommendations

Some of the future works that can be researched with this thesis as a base are listed as follows:

- The Simulink model developed for this research work can be used to perform Hardware-in-the-loop (HIL) testing of the battery pack to analyse and understand the performance and battery life over the entire BEV operation. The main output of the model is the power drawn from or fed into the battery which is in turn used to calculate the energy. This signal can be used by a bi-directional power supply to emulate an actual heavy-duty BEV.
- Designing and developing motors in-house specifically for the heavy-duty application can help improve the energy efficiency of the BEV. When exploring the option of motor design, this model will provide insight into the frequent operating points of the motor and the contribution of each individual loss based on the driving profile information. Range improvement can be achieved with new motor design such that the motor operates in a high-efficiency region most of the time over the entire drive cycle.

- With respect to the powertrain architectures, this model addresses the improvements in energy efficiency that different powertrains can provide in comparison to the single-motor fixed gear powertrain. However, the optimisation challenges involved in the development of these powertrains are merely stated and not addressed here. Hence, the suggested powertrain architectures can be optimised to improve energy efficiency in future work.
- It would be interesting to include a thermal model and cooling system to observe heat dissipation during motor operation especially due to permanent magnets and its effects on energy efficiency.
- Another parameter of importance that can strongly influence the decision of powertrain besides energy efficiency is the cost of implementation. Hence, this parameter could be further investigated.

7.3. Hardware-in-the-loop (HIL) testing

Hardware-in-the-loop (HIL) testing is a technique used to facilitate rapid prototyping and test advanced systems with real-time simulations [82]. The reason why HIL testing is necessary is that this approach helps to obtain results that are close to what can be expected in the final product thereby minimising cost and enhancing reliability. This testing can be used to perform tests with extreme use cases that could potentially be detrimental in real situations.

In this testing, a powertrain model with mathematical representation, such as the models developed in this thesis, can replace the physical system and test the battery packs of future BEVs. The forward-facing model helps in addressing the important dynamics of the physical model [10]. In this section, the possible HIL test bench for future battery testing is discussed.

7.3.1. HIL Test Bench Setup Proposal

The HIL test bench is proposed with the focus on testing the battery pack using the powertrain model. To realise this testing, three components are required namely a simulator, a power amplifier, and the device-under-test. Figure 7.1 shows the layout of the test bench. Here, the device-under-test is the battery pack that will be developed for the BEV.

The simulator is a low-latency real-time computing platform that simulates the physical system responses [82]. A dSPACE SCALEXIO simulator can be used for this HIL application as it provides advantages such as scalability, high-performance processor, fast I/O capabilities, etc [83]. More studies can be conducted to choose the most suitable depending on the preferred testing location such as in-vehicle or laboratory, the required number of ports based on future testing, etc. The simulator will run the developed model and provide the information regarding the power draw from the battery during driving conditions and power recuperated during braking. This information is utilised by the power amplifier to draw or feed power from or to the battery respectively.

The power amplifier that is recommended for this application is a bi-directional power supply which will emulate the entire drivetrain. During braking conditions, the bi-directional power supply draws AC power from the grid and rectifies to DC power to charge the battery and during driving conditions, the DC power from the battery is converted to AC power and fed back to the grid. Thus based on the budget and the size of the battery pack to be tested, the component and its size can be selected for the test bench.

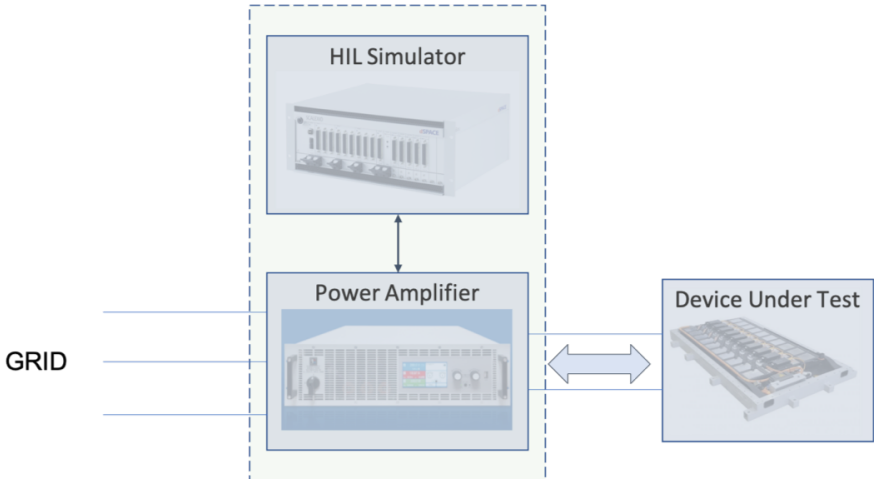

Figure 7.1: HIL test bench layout

Bibliography

[1] United State Environmental Protection Agency. (2017, July) Fast facts: US transportation sector greenhouse gas emissions. [Online]. Available: https://nepis.epa.gov/Exe/ZyPDF.cgi?Dockey=P100S7NK.pdf

[2] Union of Concerned Scientists. (2018, July) Cars, trucks, buses and air pollution. [Online]. Available: https://www.ucsusa.org/clean-vehicles/vehicles-air-pollution-and-human-health/cars-trucks-air-pollution

[3] T. Earl, L. Mathieu, S. Cornelis, S. Kenny, C. C. Ambel, and J. Nix, "Analysis of long haul battery electric trucks in EU," in *Commercial Vehicle Workshop, Graz*, 2018, p. 22.

[4] Green Car Congress. (2020) DAF trucks showcases electric and hybrid trucks at IAA CV. [Online]. Available: https://www.greencarcongress.com/2018/09/20180927-daf.html

[5] Torque Agency Group. (2018, Sep.) Continental and DAF present new innovations at IAA 2018 • Torque Agency Group. [Online]. Available: https://www.torqueagencygroup.com/continental-and-daf-new-innovations-at-iaa-2018/

[6] C. Chan, "The state of the art of electric and hybrid vehicles," *Proceedings of the IEEE*, vol. 90, no. 2, pp. 247–275, Feb. 2002.

[7] W. Hucho and G. Sovran, "Aerodynamics of road vehicles," *Annual review of fluid mechanics*, vol. 25, no. 1, pp. 485–537, 1993.

[8] J. Y. Wong, *Theory of Ground Vehicles*, 4th ed. John Wiley & Sons, Inc., 2008.

[9] T. D. Gillespie, *Fundamentals Of Vehicle Dynamics*, 1st ed. Society of Automotive Engineers, Inc., 1992.

[10] F. Assadian, G. Mohan, and S. Longo, "Comparative analysis of forward-facing models vs backward-facing models in powertrain component sizing," in *Hybrid and Electric Vehicles Conference 2013 (HEVC 2013)*. London, UK: Institution of Engineering and Technology, 2013, pp. 10.7–10.7. [Online]. Available: https://digital-library.theiet.org/content/conferences/10.1049/cp.2013.1920

[11] K. Wipke, M. Cuddy, and S. Burch, "ADVISOR 2.1: a user-friendly advanced powertrain simulation using a combined backward/forward approach," *IEEE Transactions on Vehicular Technology*, vol. 48, no. 6, pp. 1751–1761, Nov. 1999.

[12] W. Xiong, Y. Zhang, and C. Yin, "Optimal energy management for a series–parallel hybrid electric bus," *Energy Conversion and Management*, vol. 50, no. 7, pp. 1730–1738, Jul. 2009. [Online]. Available: http://www.sciencedirect.com/science/article/pii/S019689040900096X

[13] B. Naourez, R. Abdelmoula, M. Chaieb, and R. Neji, "Permanent magnet motor efficiency map calculation and small electric vehicle consumption optimization," *Journal of Electrical Systems*, vol. 14, pp. 127–147, Jun. 2018.

[14] Aaron Brooker, Matthew Zolot, Terry Hendricks, Valerie Johnson, Kenneth Kelly, Bill Kramer, Tony Markel, Michael O'Keefe, Sam Sprik, Keith Wipke, and Matthew Zolot, "ADVISOR Documentation," Mar. 2013. [Online]. Available: http://adv-vehicle-sim.sourceforge.net/advisor_doc.html

[15] K. Guo and P. S. Fancher, "Preview-follower method for modelling closed-loop vehicle directional control," 1983.

[16] R. Bojoi, E. Armando, M. Pastorelli, and K. Lang, "Efficiency and loss mapping of AC motors using advanced testing tools," in *2016 XXII International Conference on Electrical Machines (ICEM)*, Sep. 2016, pp. 1043–1049.

[17] A. Mahmoudi, W. L. Soong, G. Pellegrino, and E. Armando, "Efficiency maps of electrical machines," in *2015 IEEE Energy Conversion Congress and Exposition (ECCE)*. Montreal, QC, Canada: IEEE, Sep. 2015, pp. 2791–2799. [Online]. Available: http://ieeexplore.ieee.org/document/7310051/

[18] S. Williamson, M. Lukic, and A. Emadi, “Comprehensive drive train efficiency analysis of hybrid electric and fuel cell vehicles based on motor-controller efficiency modeling,” *IEEE Transactions on Power Electronics*, vol. 21, no. 3, pp. 730–740, May 2006.

[19] G. Wu, X. Zhang, and Z. Dong, “Powertrain architectures of electrified vehicles: Review, classification and comparison,” *Journal of the Franklin Institute*, vol. 352, no. 2, pp. 425–448, Feb. 2015. [Online]. Available: http://www.sciencedirect.com/science/article/pii/S0016003214001288

[20] M. Ehsani, Y. Gao, and A. Emadi, *Modern Electric, Hybrid Electric, and Fuel Cell Vehicles: Fundamentals, Theory, and Design, Second Edition*, 2nd ed. CRC Press, Sep. 2009.

[21] H. Stenvall, “Driving resistance analysis of long haulage trucks at volvo,” Master’s thesis, Chalmers University of Technology, Göteborg, Sweden, 2010. [Online]. Available: http://publications.lib.chalmers.se/records/fulltext/133658.pdf

[22] DAF Trucks N.V. (2020) Electric & hybrid trucks - DAF Trucks N.V. [Online]. Available: https://www.daf.com:443/en/AboutDAF/Innovation/Electricandhybridtrucks

[23] ——. (2020) DAF TRUCK CONFIGURATOR. [Online]. Available: https://www.daf.co.uk:443/en-GB/Trucks/3DDAFTruckConfigurator

[24] C. C. Chan and K. T. Chau, “An overview of power electronics in electric vehicles,” *IEEE Transactions on Industrial Electronics*, vol. 44, no. 1, pp. 3–13, 1997.

[25] W. Wang, Z. Zhang, J. Shi, C. Lin, and Y. Gao, “Optimization of a Dual-Motor Coupled Powertrain Energy Management Strategy for a Battery Electric Bus Based on Dynamic Programming Method,” *IEEE Access*, vol. 6, pp. 32 899–32 909, 2018.

[26] A. Hajduga, “Dual Motor Single Shaft Powertrain Concept,” in *2018 23rd International Conference on Methods Models in Automation Robotics (MMAR)*, Warsaw University of Technology, Narbutta 84, Warsaw, 02-524, Aug. 2018, pp. 843–848.

[27] C. Rossi, D. Pontara, M. Bertoldi, and D. Casadei, “Two-motor, Two-axle Traction System for Full Electric Vehicle,” *World Electric Vehicle Journal*, vol. 8, no. 1, pp. 25–39, Mar. 2016. [Online]. Available: https://www.mdpi.com/2032-6653/8/1/25

[28] T. Abels and S. Puschel, “Vehicle drive with two electric motors,” US Patent US3 870 935A, Mar., 1975. [Online]. Available: https://patents.google.com/patent/US3870935/en

[29] M. J. Hancock, R. A. Williams, E. Fina, and M. C. Best, “Yaw motion control via active differentials:,” *Transactions of the Institute of Measurement and Control*, Jul. 2016. [Online]. Available: https://journals.sagepub.com/doi/10.1177/0142331207069489

[30] L. De Novellis, A. Sorniotti, P. Gruber, and A. Pennycott, “Comparison of Feedback Control Techniques for Torque-Vectoring Control of Fully Electric Vehicles,” *IEEE Transactions on Vehicular Technology*, vol. 63, no. 8, pp. 3612–3623, Oct. 2014.

[31] A. T. v. Zanten, R. Erhardt, and G. Pfaff, “VDC, The Vehicle Dynamics Control System of Bosch,” SAE International, Warrendale, PA, SAE Technical Paper 950759, Feb. 1995. [Online]. Available: https://www.sae.org/publications/technical-papers/content/950759/

[32] Y. Wang and D. Sun, “Powertrain Matching and Optimization of Dual-Motor Hybrid Driving System for Electric Vehicle Based on Quantum Genetic Intelligent Algorithm,” *Discrete Dynamics in Nature and Society*, vol. 2014, Nov. 2014.

[33] M. Hu, J. Zeng, S. Xu, C. Fu, and D. Qin, “Efficiency Study of a Dual-Motor Coupling EV Powertrain,” *IEEE Transactions on Vehicular Technology*, vol. 64, no. 6, pp. 2252–2260, Jun. 2015.

[34] D. Kostic Perovic, “Making the Impossible, Possible – Overcoming the Design Challenges of In Wheel Motors,” *World Electric Vehicle Journal*, vol. 5, pp. 514–519, Jun. 2012.

[35] Protean Electric. (2020) Homepage. [Online]. Available: https://www.proteanelectric.com/

[36] Elaphe Propulsion Technologies Ltd. (2020) Solutions. [Online]. Available: http://in-wheel.com/en/

[37] Gem Motors. (2020) In-wheel motors and electric drive solutions. [Online]. Available: https://gemmotors.si/

[38] Q. Ren, D. Crolla, and A. Morris, “Effect of transmission design on Electric Vehicle (EV) performance,” in *2009 IEEE Vehicle Power and Propulsion Conference*, Sep. 2009, pp. 1260–1265.

[39] A. Turner and C. Cavallino, “Multi-speed EV/FCV transmission with seamless gearshift,” in *2009 CTI Conference*, 2009.

[40] A. Sorniotti, T. Holdstock, G. L. Pilone, F. Viotto, S. Bertolotto, M. Everitt, R. J. Barnes, B. Stubbs, and M. Westby, “Analysis and simulation of the gearshift methodology for a novel two-speed transmission system for electric powertrains with a central motor:,” *Proceedings of the Institution of Mechanical Engineers, Part D: Journal of Automobile Engineering*, Jan. 2012. [Online]. Available: https://journals.sagepub.com/doi/10.1177/0954407011431415

[41] G. Wu, X. Zhang, and Z. Dong, “Impacts of Two-Speed Gearbox on Electric Vehicle’s Fuel Economy and Performance,” SAE International, Warrendale, PA, SAE Technical Paper 2013-01-0349, Apr. 2013. [Online]. Available: https://www.sae.org/publications/technical-papers/content/2013-01-0349/

[42] A. Sorniotti, M. Boscolo, A. Turner, and C. Cavallino, “Optimization of a multi-speed electric axle as a function of the electric motor properties,” in *2010 IEEE Vehicle Power and Propulsion Conference*, Sep. 2010, pp. 1–6.

[43] B. Eberleh and T. Hartkopf, “A high speed induction machine with two-speed transmission as drive for electric vehicles,” in *International Symposium on Power Electronics, Electrical Drives, Automation and Motion, 2006. SPEEDAM 2006.*, May 2006, pp. 249–254.

[44] B. Bilgin, J. Liang, M. V. Terzic, J. Dong, R. Rodriguez, E. Trickett, and A. Emadi, “Modeling and Analysis of Electric Motors: State-of-the-Art Review,” *IEEE Transactions on Transportation Electrification*, vol. 5, no. 3, pp. 602–617, Sep. 2019. [Online]. Available: https://ieeexplore.ieee.org/document/8772178/

[45] J. Larminie and J. Lowry, *Electric Vehicle Technology Explained*, 2nd ed. John Wiley & Sons, Inc., Sep. 2012.

[46] Q. Guo, Z. Chengming, L. Li, J. Zhang, and M. Wang, “Maximum Efficiency per Torque Control of Permanent-Magnet Synchronous Machines,” *Applied Sciences*, vol. 6, p. 425, Dec. 2016.

[47] R. Ni, D. Xu, G. Wang, L. Ding, G. Zhang, and L. Qu, “Maximum Efficiency Per Ampere Control of Permanent-Magnet Synchronous Machines,” *IEEE Transactions on Industrial Electronics*, vol. 62, no. 4, pp. 2135–2143, Apr. 2015.

[48] A. Boglietti, A. Cavagnino, M. Lazzari, and M. Pastorelli, “Predicting iron losses in soft magnetic materials with arbitrary voltage supply: an engineering approach,” *IEEE Transactions on Magnetics*, vol. 39, no. 2, pp. 981–989, Mar. 2003.

[49] F. Fiorillo and A. Novikov, “An improved approach to power losses in magnetic laminations under non-sinusoidal induction waveform,” *IEEE Transactions on Magnetics*, vol. 26, no. 5, pp. 2904–2910, Sep. 1990.

[50] J. Kennedy and R. Eberhart, “Particle swarm optimization,” in *Proceedings of ICNN’95 - International Conference on Neural Networks*, vol. 4, Nov. 1995, pp. 1942–1948 vol.4.

[51] R. Eberhart and J. Kennedy, “A new optimizer using particle swarm theory,” in *MHS’95. Proceedings of the Sixth International Symposium on Micro Machine and Human Science*, Oct. 1995, pp. 39–43.

[52] B. Choudhury, S. Manickam, and R. M. Jha, “Particle Swarm Optimization for Multiband Metamaterial Fractal Antenna,” *Journal of Optimization*, vol. 2013, p. 989135, Apr. 2013, publisher: Hindawi Publishing Corporation. [Online]. Available: https://doi.org/10.1155/2013/989135

[53] D. Peng, Y. Zhang, C. Yin, and J. Zhang, “Combined control of a regenerative braking and antilock braking system for hybrid electric vehicles,” *International Journal of Automotive Technology*, vol. 9, pp. 749–757, Jan. 2008.

[54] B. J. Varocky, “Benchmarking of regenerative braking for a fully electric car,” January 2011, internship report, Dept. of Mechanical Engineering, Eindhoven University of Technology and Integrated Safety Department, TNO Automotive.

[55] B. Xiao, H. Lu, H. Wang, J. Ruan, and N. Zhang, “Enhanced Regenerative Braking Strategies for Electric Vehicles: Dynamic Performance and Potential Analysis,” *Energies*, vol. 10, no. 11, p. 1875, Nov. 2017. [Online]. Available: http://www.mdpi.com/1996-1073/10/11/1875

[56] G. Lutzemberger, “Cycle life evaluation of lithium cells subjected to micro-cycles,” in *2015 5th International Youth Conference on Energy (IYCE)*. Pisa, Italy: IEEE, May 2015, pp. 1–5. [Online]. Available: http://ieeexplore.ieee.org/document/7180788/

[57] Green Car Congress. (2013, Feb.) Siemens to collaborate more closely with Semikron on automotive power electronics; takes over Semikron subsidiary. [Online]. Available: https://www.greencarcongress.com/2013/02/siemens-20130222.html

[58] N. Mohan, T. M. Undeland, and W. P. Robbins, *Power electronics: converters, application and design*. John Wiley & Sons, inc, 2003.

[59] (2020, May) SKiM600GD126DLM | SEMIKRON. [Online]. Available: https://www.semikron.com/products/product-classes/igbt-modules/detail/skim600gd126dlm-23916180.html

[60] V. Dos Santos, B. Cougo, N. Roux, B. Sareni, B. Revol, and J.-P. Carayon, “Trade-off between Losses and EMI Issues in Three-Phase SiC Inverters for Aircraft Applications,” in *EMC 2017 International Conference*. Washington DC, United States: IEEE, Aug. 2017. [Online]. Available: https://hal.archives-ouvertes.fr/hal-01588886

[61] E. Gurpinar, R. Wiles, B. Ozpineci, T. Raminosoa, F. Zhou, Y. Liu, and E. M. Dede, “SiC MOSFET-Based Power Module Design and Analysis for EV Traction Systems,” in *2018 IEEE Energy Conversion Congress and Exposition (ECCE)*, Sep. 2018, pp. 1722–1727.

[62] A. Wintrich, U. Nicolai, W. Tursky, and T. Reimann, *Application manual power semiconductors*, 2nd ed. Ilmenau: ISLE Verlag, 2015.

[63] “Application Notes | Toshiba Electronic Devices & Storage Corporation | Asia-English.” [Online]. Available: https://toshiba.semicon-storage.com/ap-en/semiconductor/knowledge/application-note.html

[64] L. Mestha and P. Evans, “Analysis of on-state losses in PWM inverters,” *IEE Proceedings B - Electric Power Applications*, vol. 136, no. 4, pp. 189–195, Jul. 1989.

[65] E. A. Grunditz and T. Thiringer, “Modelling and scaling procedure of a vehicle electric drive system,” *Report, Chalmers University of Technology, Sweden, url: https://research. chalmers. se/en/publication*, p. 19, 2017.

[66] J. Landivar Lopez, “Hardware in the Loop Simulation of an Electric Vehicle Powertrain,” Master’s thesis, TU Delft, Delft, Netherlands, 2019. [Online]. Available: https://repository.tudelft.nl/islandora/object/uuid%3A826849d2-32e1-400a-a7a3-de1b9201d97a

[67] S. Morimoto, Y. Takeda, T. Hirasa, and K. Taniguchi, “Expansion of operating limits for permanent magnet motor by current vector control considering inverter capacity,” *IEEE Transactions on Industry Applications*, vol. 26, no. 5, pp. 866–871, Sep. 1990.

[68] The Mathworks, Inc. (2020, July) Parameterize a Permanent Magnet Synchronous Motor - MATLAB & Simulink - MathWorks Benelux. [Online]. Available: https://nl.mathworks.com/help/physmod/sps/examples/parameterize-a-permanent-magnet-synchronous-motor.html

[69] F. Campolongo, A. Saltelli, and J. Cariboni, “From screening to quantitative sensitivity analysis. A unified approach,” *Computer Physics Communications*, vol. 182, no. 4, pp. 978–988, Apr. 2011. [Online]. Available: http://www.sciencedirect.com/science/article/pii/S0010465510005321

[70] J. Asamer, A. Graser, B. Heilmann, and M. Ruthmair, “Sensitivity analysis for energy demand estimation of electric vehicles,” *Transportation Research Part D: Transport and Environment*, vol. 46, pp. 182–199, Jul. 2016. [Online]. Available: https://linkinghub.elsevier.com/retrieve/pii/S1361920915300250

[71] C. De Cauwer, J. Van Mierlo, and T. Coosemans, “Energy Consumption Prediction for Electric Vehicles Based on Real-World Data,” *Energies*, vol. 8, no. 8, pp. 8573–8593, Aug. 2015. [Online]. Available: http://www.mdpi.com/1996-1073/8/8/8573

[72] H. Bauer, A. Cypra, A. Beer, and Robert Bosch GmbH, *Automotive handbook*, 4th ed. Stuttgart; Warrendale, PA.: Robert Bosch ; Distribution, Society of Automotive Engineers, 1996.

[73] E. L. Bianchi, “Design and evaluation of powertrain architectures for battery electric vehicles,” Master’s thesis, TU Delft, Delft, Netherlands, 2016. [Online]. Available: https://repository.tudelft.nl/islandora/object/uuid%3Aab11f09e-3e1f-47a0-9f7a-14e8fd61bdce

[74] N. Pettersson and K. H. Johansson, “Modelling and control of auxiliary loads in heavy vehicles,” *International Journal of Control*, vol. 79, no. 5, pp. 479–495, May 2006. [Online]. Available: https://www.tandfonline.com/doi/full/10.1080/00207170600587333

[75] C. Andersson, “On Auxiliary Systems in Commercial Vehicles,” Ph.D. dissertation, Lunds universitet, Lund, Sweden, 2016. [Online]. Available: https://portal.research.lu.se/ws/files/5907461/716038.pdf

[76] P. Arora, “Capacity Fade Mechanisms and Side Reactions in Lithium-Ion Batteries,” *Journal of The Electrochemical Society*, vol. 145, no. 10, p. 3647, 1998. [Online]. Available: https://iopscience.iop.org/article/10.1149/1.1838857

[77] (2020, June) How to find tyre size? | Help Centre | Blackcircles.com. [Online]. Available: https://www.blackcircles.com/helpcentre/tyres/how-do-i-find-my-tyre-size

[78] Z. Stevic and I. Radovanovic, “Energy Efficiency of Electric Vehicles,” *New Generation of Electric Vehicles*, Dec. 2012. [Online]. Available: https://www.intechopen.com/books/new-generation-of-electric-vehicles/energy-efficiency-of-electric-vehicles

[79] Shaheer Anwer. (2020, Mar.) How Wheel Size Affect Efficiency And Performance In Electric Cars? [Online]. Available: https://fossbytes.com/how-wheel-size-affect-efficiency-and-performance-in-electric-cars/

[80] D. W. Gao, C. Mi, and A. Emadi, “Modeling and Simulation of Electric and Hybrid Vehicles,” *Proceedings of the IEEE*, vol. 95, no. 4, pp. 729–745, Apr. 2007.

[81] T. Hofman, M. Steinbuch, R. van Druten, and A. F. A. Serrarens, “Design of CVT-Based Hybrid Passenger Cars,” *IEEE Transactions on Vehicular Technology*, vol. 58, no. 2, pp. 572–587, Feb. 2009.

[82] J. J. Poon, M. A. Kinsy, N. A. Pallo, S. Devadas, and I. L. Celanovic, “Hardware-in-the-loop testing for electric vehicle drive applications,” in *2012 Twenty-Seventh Annual IEEE Applied Power Electronics Conference and Exposition (APEC)*, Feb. 2012, pp. 2576–2582.

[83] dSPACE GmbH. (2020, July) SCALEXIO. [Online]. Available: https://www.dspace.com/en/inc/home/products/hw/simulator_hardware/scalexio.cfm